A Broadband Rectenna Array for RF Energy Recycling

by

Florian B. Helmbrecht

Diplomarbeit

Written at the

University of Colorado at Boulder,

submitted to the

Technische Universität München

in Partial Fulfillment of the

Requirements for the Degree of

Diplom-Ingenieur (TU-München)

Technische Universität München

September 2002

A Broadband Rectenna Array for RF Energy Recycling

Florian B. Helmbrecht
Technische Universität München, 2002

Supervisor:
Prof. Zoya Popović,
University of Colorado at Boulder
Prof. Erwin Biebl,
Technische Universität München

In this work, an 8 by 8 element rectenna array for very low incident power levels and a broad bandwidth is investigated. The concepts and simulations used were verified with a matched RF-rectifier and a single element rectenna.

Contents

Abstract ii

List of Figures v

List of Tables vii

Chapter 1 Introduction 1

Chapter 2 Verification of the Agilent ADS HB-Simulation 3

2.1 Harmonic Balance Simulation 3

2.2 Design on Agilent ADS 5

2.2.1 Lumped Component Rectifier 6

2.2.2 Distributed Component Rectifier 7

2.3 Calibration and Measurement 8

2.3.1 Calibration 8

2.3.2 Measurement 9

2.4 Modeling Parasitic Effects in the Simulation 10

Chapter 3 A Single Rectenna 15

3.1 Spiral Antennas 15

3.1.1 Design 16

3.1.2 Simulation 17

3.2 Simulations on the Rectenna 22
3.2.1 Antenna Model in Circuit Simulation 22
3.2.2 The Rectifier 23
3.2.3 Verification 23
3.2.4 Optimal Antenna Impedance 26
3.2.5 The Choice of the Diode 26
3.3 Measurements on the Rectenna 31
3.3.1 Measurement Setup and Limitations 31
3.3.2 Efficiency versus Incident Power 34
3.3.3 Polarization 36
3.3.4 3D DC Pattern 37
3.3.5 Reradiation of Harmonics 37

Chapter 4 A Rectenna Array **41**
4.1 Design 41
4.1.1 2 by 2 Elements Array 41
4.1.2 4 by 4 Elements Sub-Array 42
4.1.3 8 by 8 Elements Array 43
4.2 Measurements 43
4.2.1 3D DC Pattern of the 2 by 2 Elements Array 43
4.2.2 3D DC Pattern of the 8 by 8 Elements Array 44
4.2.3 Broadside Power Sweep Comparison 44

Chapter 5 Conclusion and Future Work **49**

List of Figures

2.1 Rectifier circuit diagram 5
2.2 Layout of 2.5 GHz lumped element rectifier 7
2.3 Layout of 2.5 GHz distributed rectifier 8
2.4 Calibration and measurement 9
2.5 Efficiency vs. load resistance (lumped components) 11
2.6 Reflected power vs. frequency (lumped components) 11
2.7 Efficiency vs. load resistance (distributed components) 12
2.8 Reflected power vs. frequency (distributed components) 12
2.9 Equivalent circuit for inductor with parasitics 13
2.10 Equivalent circuit for capacitor with parasitics 13

3.1 Dimensions and parameters of a spiral 16
3.2 ΔS Comparison I 20
3.3 ΔS Comparison II 20
3.4 Smith chart for spiral antennas 21
3.5 The ADS antenna model 24
3.6 The rectification circuit 24
3.7 Vivaldi rectenna measurement and simulation 27
3.8 Spiral rectenna measurement and simulation 27
3.9 Efficiency of a diode vs. various parameters 29
3.10 Sensitivity to mismatch 29

3.11 Comparison of the Diodes 32
3.12 Measurement setup in the anechoic chamber 32
3.13 Hemisphere with 648 points ($N_\varphi = 50$, $N_\vartheta = 20$), constant spacing . 35
3.14 Efficiency versus incident power (ads3) 35
3.15 Polarization of spiral ads3 36
3.16 DC pattern of spiral ads3 at 3 GHz 38
3.17 DC pattern of spiral ads3 at 6 GHz 38
3.18 Spectrum of the reradiated power (spiral ads3) 40
3.19 Distribution of the power on the 3rd harmonic 40

4.1 Dimensions of the 2×2 array 42
4.2 Layout of the 8×8 array 44
4.3 3D DC pattern of the 2×2 array at 3 GHz 45
4.4 3D DC pattern of the 2×2 array at 6 GHz 45
4.5 3D DC pattern of the 8×8 array at 3 GHz 46
4.6 3D DC pattern of the 8×8 array at 6 GHz 46
4.7 Comparison of DC output power vs. power density 48

List of Tables

2.1 MA4E2054 parameters, as given in manufacturer's specifications . . 6
2.2 Z_0, λ, and w for given substrate 6

3.1 Simulated Spiral Antennas 18
3.2 Lower frequency limits 22
3.3 Diode parameters, as given in manufacturer's specifications 30

Chapter 1

Introduction

Today where more and more devices become wireless, those seem to be independent from wires; but in fact this is only true when they are in use, i.e. transmitting information. Those devices still require wires from time to time, either direct when batteries are recharged or indirect when batteries are exchanged. Perhaps this is not a great disadvantage for devices such as cell phones; but where it comes to wireless sensors, today's situation requires maintenance which is time consuming and therefore expensive. In the work presented here, the focus is on low power and broadband rectifying antennas, i.e. rectennas, which are able to receive and rectify RF radiation that is available from a wide range of transmitters, such as mobile communication systems. These rectennas might be able to recharge batteries that supply those sensors that transmit information only from time to time and only at low power, e.g. smoke detectors distributed over a building complex.

Rectennas can also be used as receivers for power transmission typically at a high power level at a given frequency, e.g. between rotating parts of satellites. The rectennas investigated in this work might not be the best choice for these applications because of the missing matching network between diode and antenna, which can lead to high losses through re-radiation.

Thinking of extreme high frequencies in the THz region, rectennas that col-

lect light might be an alternative to solar cells. These frequencies would require extremely fast diodes as well as extremely small antennas on the order of 1 μm.

This work contains methods to simulate rectennas with Harmonic Balance and electromagnetic full-wave simulators. The rectennas investigated here, do not have matching networks or filtering sections due to the broad bandwidth that the rectennas are supposed to cover. An array structure is also proposed to increase the total DC output power.

Chapter 2

Verification of the Agilent ADS HB-Simulation

This chapter describes the simulations and measurements on a 2.5 GHz lumped component and a 2.5 GHz distributed rectifier. The results of the nonlinear Agilent ADS Harmonic Balance (HB) Simulations of diode rectifiers were compared with measurements in order to assess the usefulness of the simulation tool for rectifier design.

2.1 Harmonic Balance Simulation

For analyzing nonlinear circuits, two major techniques are known: the time domain based large signal - small signal and the frequency domain based harmonic balance analysis. Since this research only applies single tone excitation to circuits, the decision was made to use the harmonic balance method. This also has the advantage of avoiding time constants, which are much greater than the inverse of the excitation frequency and require integration over many periods. These can differ from each other by several orders of magnitude, which would cause problems for numerical solvers of the nonlinear differential equations.

HB analysis is performed in the frequency domain Fourier space, thus avoiding differential equations. The entire circuit is split up into a linear and a nonlinear sub-circuit connected by N ports. Because the nonlinear devices create harmonics, the port-voltages must not only be known for the sinusoidal fundamental frequency of the excitation, but for all harmonics $k = 1 \dots K$, up to a given cut-off. For the entire circuit, assuming it is an M-port, the following systems can be written:

$$\begin{bmatrix} I_{1,k} \\ \vdots \\ I_{N,k} \\ I_{N+1,k} \\ \vdots \\ I_{M+N,k} \end{bmatrix} = \mathbf{Y}_{\text{lin}} \cdot \begin{bmatrix} U_{1,k} \\ \vdots \\ U_{N,k} \\ U_{N+1,k} \\ \vdots \\ U_{M+N,k} \end{bmatrix} \tag{2.1}$$

$$\begin{bmatrix} \hat{I}_{1,k} \\ \vdots \\ \hat{I}_{N,k} \end{bmatrix} = \hat{\mathbf{Y}}_{\text{nlin}} \cdot \begin{bmatrix} \hat{U}_{1,k} \\ \vdots \\ \hat{U}_{N,k} \end{bmatrix} \tag{2.2}$$

where $U_{m,k}$ and $I_{m,k}$ are k-th harmonics of of port voltages, or respective currents, and $\mathbf{Y}_{\text{lin}}$ and $\hat{\mathbf{Y}}_{\text{nlin}}$ are the admittance matrices of the sub-circuits. The *hat* notation relates to the nonlinear sub-circuit, whereas letters without hats belong to the linear sub-circuit. For the N connecting ports, $I_{n,k} = -\hat{I}_{n,k}$, i.e. Kirchhoff's current law, and $U_{n,k} = \hat{U}_{n,k}$, i.e. Kirchhoff's voltage law, must be satisfied for all $n = 1 \dots N$. To solve for the entire circuit, port-voltages $U_{n,k}$ have to be found, that solve both Eqs. 2.1 and 2.2, so that $I_{n,k} = -\hat{I}_{n,k}$. As soon as those voltages are found, the circuit is analyzed. A more detailed discussion on the harmonic balance technique can be found in [Maa97].

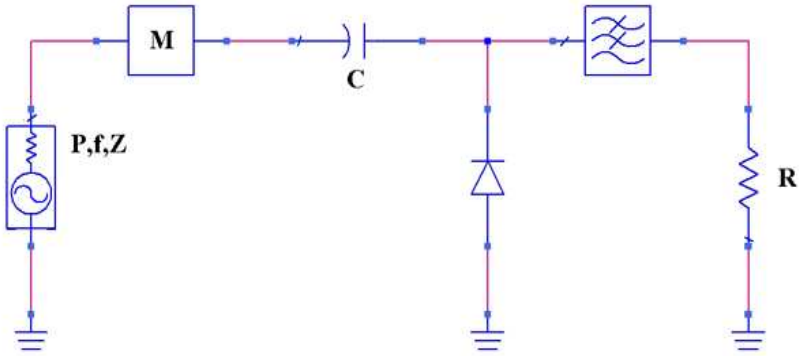

Figure 2.1: Rectifier circuit diagram, where M is a matching network, C a DC block, R the load resistance, and the source has the parameters power P, frequency f, and impedance Z

2.2 Design on Agilent ADS

The rectifiers have the basic circuit diagram shown in Fig. 2.1, where M is a matching network, C a DC block, R the load resistance, and the source has the parameters power P, frequency f, and impedance Z.

A M/ACom MA4E2054 diode is the nonlinear device of each design. The circuits are microstrip circuits that were milled on one side of a 20 mil (0.508 mm) Rogers Duroid substrate ($\epsilon_\mathrm{r} = 2.2$, $\mu_\mathrm{r} = 1$) with a 1 oz copper layer ($\frac{1\,\mathrm{oz}}{\mathrm{ft}^2} \approx 35\,\mu\mathrm{m}$) on both sides.

Both designs have a DC blocking capacitor of 1 pF, placed across a on the RF side, to make sure that DC power is fully delivered to the load. Matching the circuit impedance to the input impedance of 50 Ω is done using a single-stub matching section. All other transmission sections that appear in the ADS network, were added to optimize the distance between two elements. The length of lines (including stubs) was optimized using the ADS Nominal Optimization. The values in Tab. 2.2 were obtained from the ADS LineCalc tool and can be verified with the equations given by [Edw88]. The diode is placed across b in Figs. 2.2 and 2.3, and

Parameter		Value
saturation current	I_s	$3 \cdot 10^{-8}\,\mathrm{A}$
ohmic resistance	R_s	$11\,\Omega$
emission coefficient	N	1.05
zero bias junction capacitance	C_j0	$0.10\,\mathrm{pF}$
junction potential	V_j	$0.40\,\mathrm{V}$
grading coefficient	M	0.50
bandgap	E_g	$0.69\,\mathrm{eV}$
reverse breakdown voltage	B_v	$5.0\,\mathrm{V}$
current at B_V	I_BV	$1 \cdot 10^{-5}\,\mathrm{A}$

Table 2.1: MA4E2054 parameters, as given in manufacturer's specifications

Z_0/Ω	w/mm	$\frac{\lambda}{2}$/mm (2.5 GHz)
50	1.521	43.881
25	3.934	42.559
90	0.523	45.313

Table 2.2: Z_0, λ, and w for given substrate

connected to the bottom layer by a via, made of a piece of wire.

2.2.1 Lumped Component Rectifier

The DC side of the lumped component design is made up by a LC-lowpass filter ($L = 100\,\mathrm{nH}$, placed across c, $C = 100\,\mathrm{nF}$, placed across d). The following list was used as optimization criteria to determine the optimal lengths of the transmission lines and the stub:

1. $eff_\mathrm{min} = 0.9$
2. $r(1)_\mathrm{max} = -20\,\mathrm{dB}$
3. $r(2)_\mathrm{max} = -20\,\mathrm{dB}$

where eff is the overall efficiency and $r(n)$ is the ratio of the power reflected in the n-th harmonic to the RF input power at the fundamental frequency.

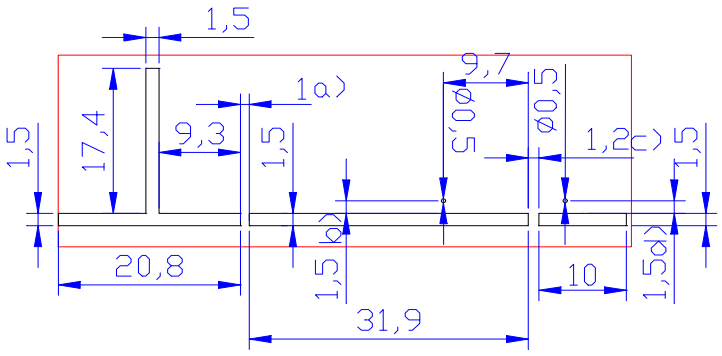

Figure 2.2: Layout of 2.5 GHz lumped element rectifier

2.2.2 Distributed Component Rectifier

The distributed lowpass filter consists of three microstrip lines of different width. First comes a piece with a width of 4 mm, $Z_0 \approx 25\,\Omega$, that behaves like a shunt capacitor for high frequencies because of its high C'. Next comes a piece with 0.5 mm, with a high $Z_0 \approx 90\,\Omega$, that behaves like a series resistor. The last part of the lowpass filter a second 4 mm microstrip line, acting as another shunt capacitor in the equivalent circuit diagram (ECD). See Tab. 2.2 for Z_0 for a given line-width. The following optimization criteria were used for Nominal Optimization:

1. $eff_{\min} = 0.9$
2. $r(1)_{\max} = -20\,\mathrm{dB}$
3. $r(2)_{\max} = -20\,\mathrm{dB}$
4. $r(3)_{\max} = -20\,\mathrm{dB}$

where the parameters have the same meaning as in the previous chapter on the lumped component rectifier.

Because a significant amount of power was reflected back at the 3rd harmonic, a second stub was added on the RF side to short the 3rd harmonic. To determine

the optimal length for that stub during optimization, the criterion of the reflected power of the 3rd harmonic was added.

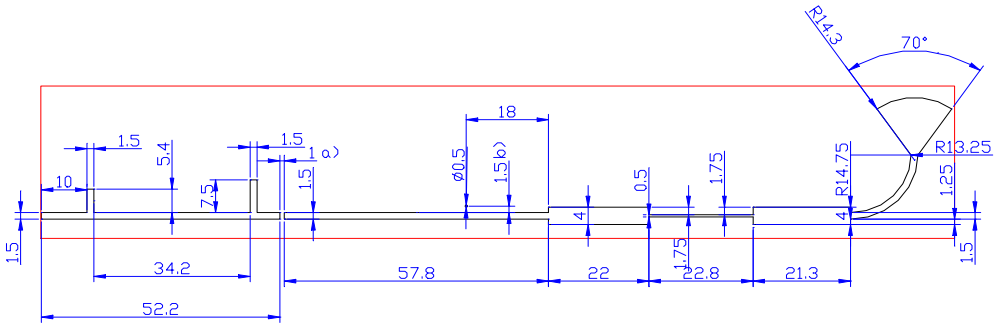

Figure 2.3: Layout of 2.5 GHz distributed rectifier

2.3 Calibration and Measurement

2.3.1 Calibration

Calibration was done for all paths, where significant losses were expected, i.e. cables and coupler. For all power level measurements with the spectrum analyzer, a resolution bandwidth of 1 kHz was used to minimize influence of the noise. The spectrum analyzer was used instead of a power meter so that the harmonics can be read out separately. Calibration was performed for the frequencies mentioned in chapter 2.3.2. First the losses from the RF source to the DUT were measured, while the -10 dB port of the coupler was terminated with a matched load (Fig. 2.4a). The attenuation for the reflected power was measured, with a short at one coupler port, for all harmonics taken into account (Fig. 2.4b) and corrected with the data measured before, so we get the attenuation from the coupler port to the spectrum analyzer input port for each harmonic.

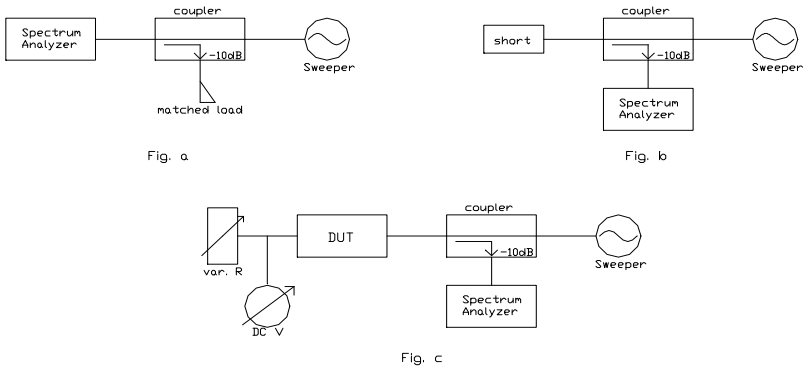

Figure 2.4: Calibration and measurement

2.3.2 Measurement

First the true optimal frequency for the circuit has to be found, which can be different from the calculated ones because of fabrication tolerances of the lumped elements and the microstrip lines. By tuning the input frequency, a maximum of the DC output voltage was found. The optimal frequency for the lumped element rectifier was at 2.288 GHz 8.5% below the design frequency, whereas the distributed rectifier frequency was at 2.327 GHz 6.9% below 2.5 GHz. The optimal frequencies were used later for all other measurements.

DC Power versus Load Resistance

Using a variable resistance, the load at the DC output was increased from 100 Ω to 1kΩ in steps of 10 Ω. The DC output power was calculated as $P_0 = \frac{U_0^2}{R_\mathrm{L}}$, "0" indicating the DC components. The overall efficiency is defined as

$$\eta_0 = \frac{P_0}{P_{\mathrm{RF_{in}}}} \tag{2.3}$$

with $P_{\mathrm{RF_{in}}} = 10\,\mathrm{dBm} - P_\mathrm{loss}$ and P_loss representing the cable and coupler losses. The maximum of this function $P_0(R_\mathrm{L})$ indicates the situation closest to the matched one, i.e. $R_\mathrm{L} = |Z_\mathrm{rect}|$. The results are plotted in Figs. 2.5 and 2.7.

Reflected Power versus Frequency

Using the system shown in Fig. 2.4c, the power of each harmonic is measured in relation to the RF input power. Because of the DC block capacitor, there is no DC component. The reflection of the rectifiers ($20 \cdot \log(S_{11})$) is shown in Figs. 2.6 and 2.8.

2.4 Modeling Parasitic Effects in the Simulation

As Figs. 2.5, 2.6, 2.7, and 2.8 show, the simulation results do not match the measured data. The deviations are caused by parasitic effects of the lumped elements. To be able to include those effects in the simulation, a more realistic circuit model should be used.

The manufacturer of the lumped inductors (Koa Speers Inc.) gives a minimum self-resonance frequency of $f_{\mathrm{sr,min}} = 700\,\mathrm{MHz}$ and a maximal DC resistance of $R_{\mathrm{DC,max}} = 0.44\,\Omega$. The tolerance of the inductance is given with 20%. So the inductor equivalent circuit diagram is shown in Fig. 2.9. From the values given above and

$$f_{\mathrm{sr}} = \frac{1}{2\pi \cdot \sqrt{LC}} \qquad \overset{f_{\mathrm{sr,min}}=700\,\mathrm{MHz}}{\Longleftrightarrow} \qquad C_{\mathrm{max}} = 0.52\,\mathrm{pF} \tag{2.4}$$

a range for the values of the elements L, R and C can be obtained. For the lumped capacitor, only an inductance was introduced to model the inductance of the connecting pins (see Fig. 2.10). The manufacturer does not give any data such as self-resonance-frequency or a Q-factor, so the typical inductance for contact wires, several nH, in numbers 0.5 to 20, was taken as the range for possible values.

These values were given to ADS as limits for the values of the parasitic elements. The optimization goals now were the measured reflection values for each harmonic taken into account.

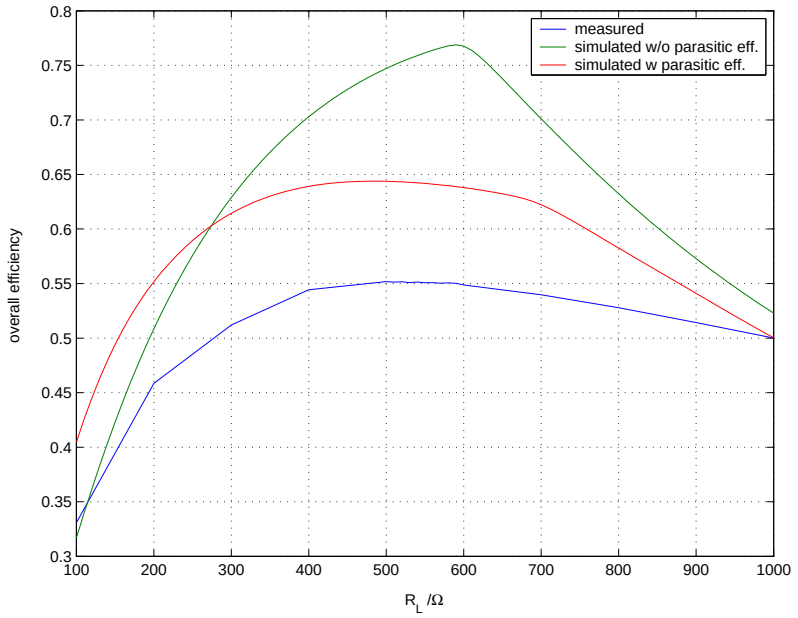

Figure 2.5: Efficiency vs. load resistance (lumped components)

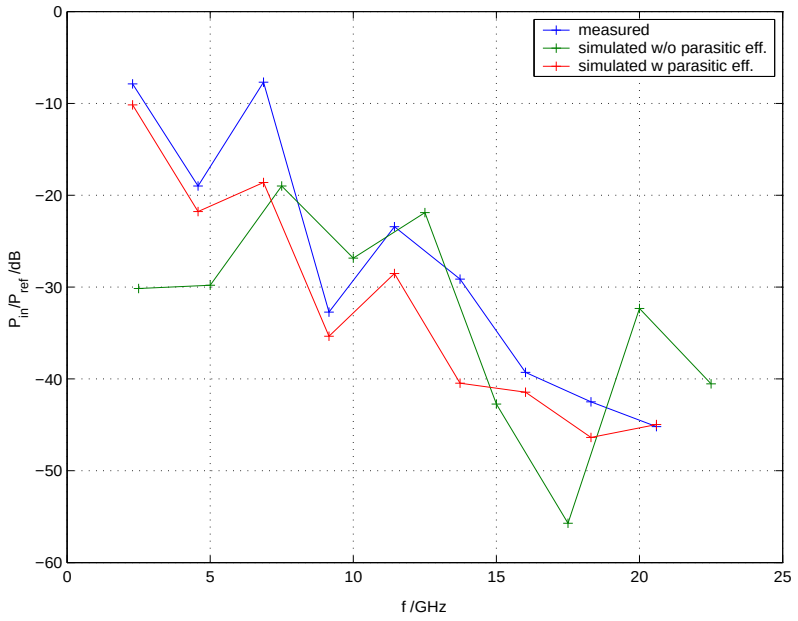

Figure 2.6: Reflected power vs. frequency (lumped components)

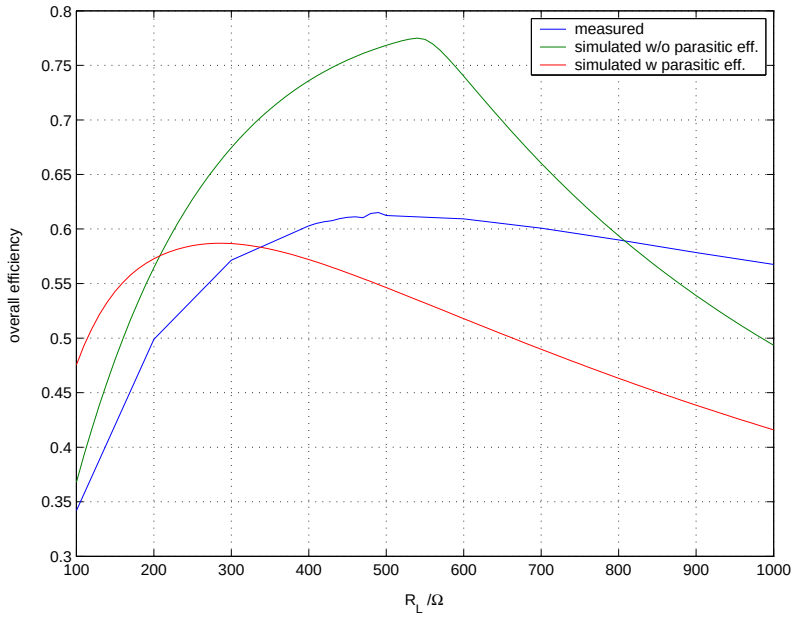

Figure 2.7: Efficiency vs. load resistance (distributed components)

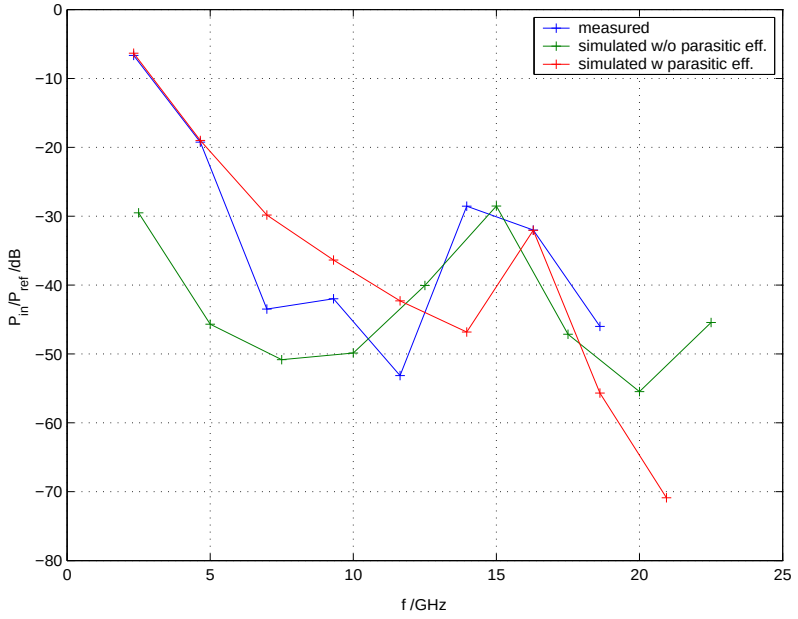

Figure 2.8: Reflected power vs. frequency (distributed components)

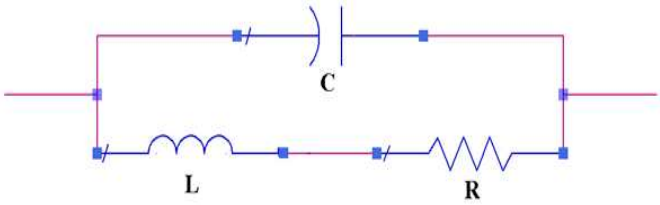

Figure 2.9: Equivalent circuit for a surface mounted chip inductor with parasitic C and R

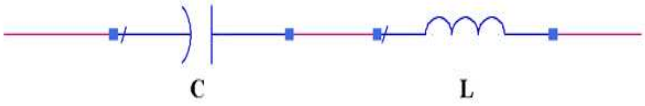

Figure 2.10: Equivalent circuit for a surface mounted chip capacitor with parasitic L

Chapter 3

A Single Rectenna

3.1 Spiral Antennas

Because of the extreme bandwidth of interest to the topic of power transmission, especially for "RF Recycling", a very broadband antenna is necessary. The efficiency of a rectifier degrades dramatically with an unmatched source. This is why a frequency independent antenna with an impedance located within the area on the smith chart bordered by the lines given by the power and frequency dependent S-parameters of the rectifier would be the first choice. The change in S-parameters over frequency for an antenna is usually much larger than for the rectifier, unless a broadband or ideally a frequency independent antenna is used. The characteristics of an antenna, i.e. impedance, gain and polarization, depend on the shape of the antenna, with the dimensions normalized to the free-space wavelength. This means, that the characteristics of an antenna do not change, if not only the dimensions, but also the wavelength is scaled by a factor K. For an equiangular spiral the following scaling equation holds:

$$K \cdot \exp\left(a \cdot (\varphi + \phi)\right) = \exp\left(a \cdot \left(\varphi + \frac{1}{a} \ln K + \phi\right)\right) \tag{3.1}$$

with φ the angle of the polar coordinates and a the scaling factor of the spiral. Furthermore, if the shape of an antenna, consisting of metal in air, is only determined by

angles, the result is a frequency independent antenna (Rumsey's principle, [Rum57]). Spirals are supposed to have a nearly frequency independent behavior between a certain lower and upper frequency, given by the finite size and feed size, respectively. An ideal self-complementary antenna, i.e. a spiral-antenna of infinite dimensions has a theoretical impedance of $Z_{\text{spiral}} = \frac{1}{2} \cdot Z_{\text{F0}} = \frac{1}{2} \cdot \sqrt{\frac{\mu_0}{\epsilon_0}} = 60\pi\,\Omega \approx 188\,\Omega$. Because of the small dimensions of the spiral at the feed point and the large bandwidth, no matching section is used as e.g. in [MFC98], [MYC92], and [YC92].

3.1.1 Design

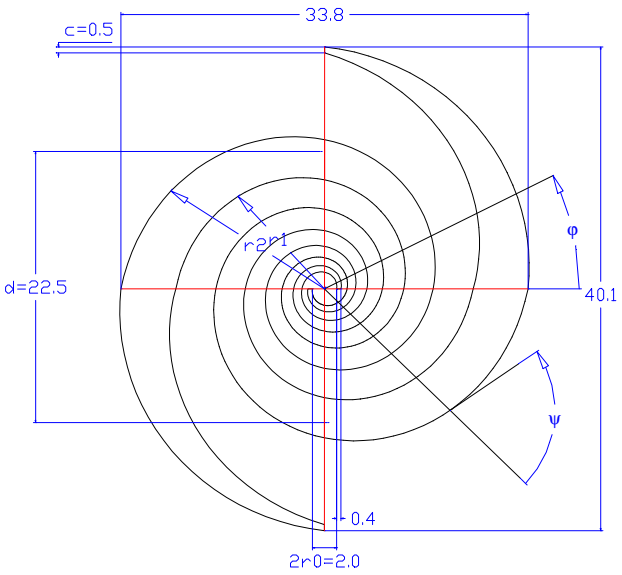

Figure 3.1: Dimensions and parameters of spiral antenna ds8 in mm

Spiral antennas, more precisely logarithmic spirals, have two or more arms, with the bordering lines being log-spiral curves as in Eq. 3.2, with r_n and φ polar coordinates, $a = \frac{1}{\tan(\psi)}$ the expansion coefficient and $|\phi_1 - \phi_2|$ the parameter, defining

the width of the arms. $\phi_{\max}$ specifies the number of turns the spiral makes.

$$r_n = r_0 \cdot \exp\left(a \cdot (\varphi + \phi_n)\right),\ n = 1, 2 \qquad \forall\, 0 \le \varphi \le \phi_{\max} \tag{3.2}$$

All the following considerations relate to two-arm spirals, which are used in this work. ϕ_1 can be set to zero because with r_0 there is another degree of freedom to control the distance of the first point of the inner line to origin. The polar coordinates for arm 1 are (r_1, φ) and (r_2, φ), whereas arm 2 is bordered by the lines $\left(r_1, \varphi - \frac{\pi}{2}\right)$ and $\left(r_2, \varphi - \frac{\pi}{2}\right)$, with φ running from 0 to the given $\phi_{\max}$. To get a self-complementary antenna, $|\Delta\phi| = |\phi_2 - \phi_1| = \frac{\pi}{2}$ needs to be obeyed. In order not to let the antennas end abruptly with a long edge, which might disturb the current distribution, the spirals used follow Eq. 3.3 for $\varphi > \phi_{\max}$. ϕ_1 is set to zero and consequently ϕ_2 is replaced by $\Delta\phi$.

$$\begin{aligned} r_{1c} &= r_0 \cdot \exp\left[a \cdot \phi_{\max} + \frac{a \cdot \varphi}{\theta_{\max}} \cdot \left(\theta_{\max} + \frac{\Delta\phi}{2} - \delta\right)\right] \qquad \forall\, \phi_{\max} < \varphi \le \theta_{\max} \\ r_{2c} &= r_0 \cdot \exp\left[a\left(\phi_{\max} + \Delta\phi\right) + \frac{a \cdot \varphi}{\theta_{\max}} \cdot \left(\theta_{\max} - \frac{\Delta\phi}{2} + \delta\right)\right] \end{aligned} \tag{3.3}$$

The δ in Eq. 3.3 is an angle derived from a parameter c (Eq. 3.4) that specifies the length of the edge at the end of each spiral arm.

$$\begin{aligned} & r_{2c}(\theta_{\max}) - r_{1c}(\theta_{\max}) \doteq c \\ \Leftrightarrow \quad & \delta = \tfrac{1}{a} \cdot \operatorname{asinh}\left\{\tfrac{c}{2 \cdot r_0} \exp\left[-a\left(\phi_{\max} + \tfrac{\Delta\phi}{2} + \theta_{\max}\right)\right]\right\} \end{aligned} \tag{3.4}$$

So the polar coordinates for $\phi_{\max} < \varphi \le \theta_{\max}$ are (r_{1c}, φ) and (r_{2c}, φ) for arm 1 and $\left(r_{1c}, \varphi - \frac{\pi}{2}\right)$ and $\left(r_{2c}, \varphi - \frac{\pi}{2}\right)$ for arm 2. All spirals simulated are shown in Tab. 3.1. None of the spirals has a ground plane because of their broadband design. Fig. 3.1 shows $ds8$, with the red lines marking symmetry axes.

3.1.2 Simulation

The simulations were done on Zeland's IE3D and Ansoft's Ensemble Method of Moments (MoM) electromagnetic simulators. In IE3D the meshing frequency was the

Antenna	r_0	a	$\phi_{\max}$	$\theta_{\max}$	$\Delta\phi$	c
ds1	1	0.25	3π	$\frac{\pi}{2}$	$\frac{\pi}{2}$	0.5
ds2	1	0.25	3π	$\frac{\pi}{2}$	$\frac{3\pi}{8}$	0.34
ds3	1	0.25	4π	$\frac{\pi}{2}$	$\frac{3\pi}{8}$	0.5
ds4	1	0.25	3π	$\frac{\pi}{2}$	$\frac{5\pi}{8}$	0.5
ds5	1	0.25	4π	$\frac{\pi}{2}$	$\frac{\pi}{2}$	0.5
ds6	1	0.25	3π	$\frac{\pi}{4}$	$\frac{\pi}{2}$	0.5
ds7	1	0.15	4π	$\frac{\pi}{2}$	$\frac{\pi}{2}$	0.3
ds8	1	0.2	4π	$\frac{\pi}{2}$	$\frac{\pi}{2}$	0.5
ds9	1	0.2	4π	$\frac{\pi}{2}$	$\frac{\pi}{2}$	0.3
ds10	1	0.25	4π	0	$\frac{\pi}{2}$	N/A
ds11	1	0.45	2π	0	$\frac{\pi}{2}$	N/A
ads3	0.6	0.25	3π	$\frac{\pi}{2}$	$\frac{\pi}{2}$	0.3

Table 3.1: Simulated Spiral Antennas

highest frequency of the concerning frequency range, with 20 cells per wavelength and the option "Automatic Edge Cell Width" turned on. This option creates a finer mesh at the edges, where the current distribution changes rapidly. In Ensemble, the meshing frequency for the fixed mesh was chosen in the middle of the frequency range, with the options "Edge mesh" and "Smooth mesh" turned on. "Edge mesh" again creates a finer mesh at the edges whereas "Smooth mesh" helps getting symmetric results for symmetric structures. All spirals were simulated using the parameters for a Rogers Duroid substrate ($\epsilon_{\mathrm{r}} = 2.2$, $\mu_{\mathrm{r}} = 1$), 20 mil (0.508 mm) thick, with a 1 oz copper layer ($\approx 35\,\mu$m). This substrate was used for those spirals that were fabricated.

Because the version of Ensemble was not set up for differential ports, two ports were used - one between each connector and ground. To convert the **S**-matrix of the 2-port into the single S_{11}-parameter of a differential 1-port, the following equations can be used. These can easily be derived, given that for a n-node network,

rank $\mathbf{Y} = n - 1$ with $\mathbf{Y} \in \mathbb{C}^{n \times n}$. Z and $\mathbf{Z}'$ are normalized.

$$\mathbf{Z}' = \left(\mathbf{1} + \mathbf{S}'\right) \cdot \left(\mathbf{1} - \mathbf{S}'\right)^{-1} \tag{3.5}$$

$$Z = Z'_{11} + Z'_{22} - Z'_{12} - Z'_{21} \tag{3.6}$$

$$S = \frac{Z - 1}{Z + 1} \tag{3.7}$$

Lower Frequency Limit

To determine the lower frequency limit for quasi-frequency independent behavior, the absolute of the difference in S_{11} of two neighboring frequency points is plotted versus frequency. All data used in this section, are results from the IE3D simulation. $\Delta S\,(f) = \left|S_{11}\left(f - \frac{\Delta f}{2}\right) - S_{11}\left(f + \frac{\Delta f}{2}\right)\right|$, with $\Delta f = 100\,\mathrm{MHz}$ being the step-width used in the simulations. It was found, that ΔS drops sharply below 0.01 around a certain frequency. This frequency can roughly be obtained from

$$\begin{aligned} \lambda'_{\mathrm{co}} &= d \cdot \pi, \qquad \epsilon'_{\mathrm{r}} = \frac{\epsilon_{\mathrm{r}} + 1}{2} \\ f_{\mathrm{co}} &= \frac{c_0}{\sqrt{\epsilon'_{\mathrm{r}}} \cdot \lambda'_{\mathrm{co}}} \end{aligned} \tag{3.8}$$

where ϵ_{r} is the dielectric constant of the substrate and d the mean diameter of the spiral at an angle π back from the end of the arms as indicated in Fig. 3.1. This angle π does not only apply to those spirals that have closing arms over this angle, but also to ds6 ($\theta_{\max} = \frac{\pi}{4}$), ds10 ($\theta_{\max} = 0$), and ds11 ($\theta_{\max} = 0$).

The two graphs of Figs. 3.2 and 3.3 show ΔS plotted versus frequency. The approximate mean diameters and the frequencies resulting from the circumference are shown in Tab. 3.2. This allows a rough estimation for the area a single spiral rectenna would take up with a given lower frequency limit. Fig. 3.4 shows the S-parameters of the spirals ds1, ds6, and ds10 over a frequency range from 2 to 10 GHz. Each trace is marked with a dot at 2 GHz and another one at its f_{co}, i.e. 4.7 GHz for ds1, 5.1 GHz for ds6, and 2.9 GHz for ds10 (see Tab. 3.2 for these values).

This behavior of the simulated antennas was found by calculating the corresponding wavelength for the cutoff frequencies on the substrate and looking for

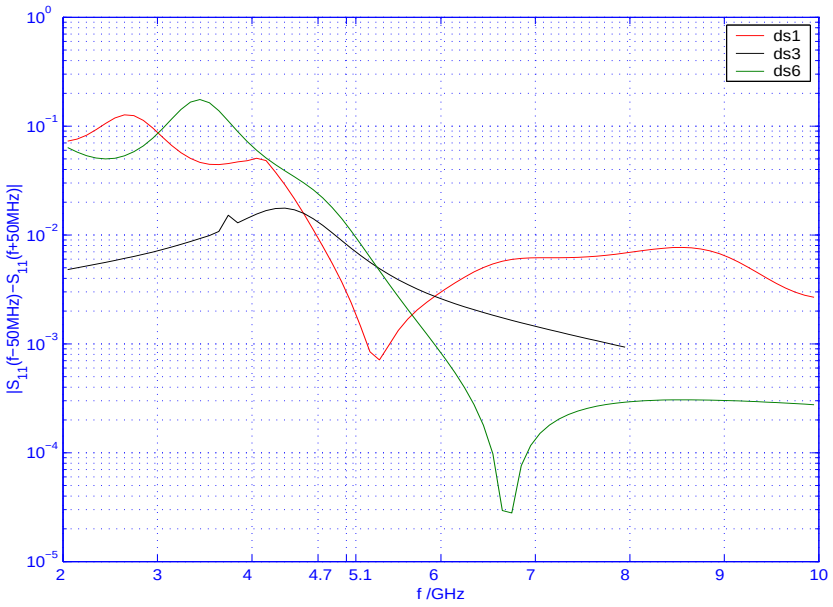

Figure 3.2: $\Delta S(f) = \left|S_{11}\left(f - \frac{\Delta f}{2}\right) - S_{11}\left(f + \frac{\Delta f}{2}\right)\right|$ of spirals ds1, ds3, ds6

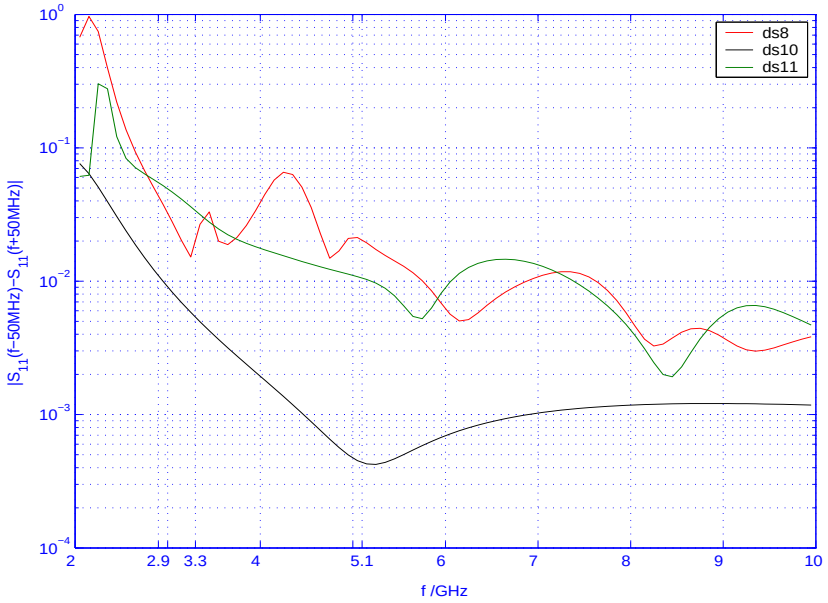

Figure 3.3: $\Delta S(f) = \left|S_{11}\left(f - \frac{\Delta f}{2}\right) - S_{11}\left(f + \frac{\Delta f}{2}\right)\right|$ of spirals ds8, ds10, ds11

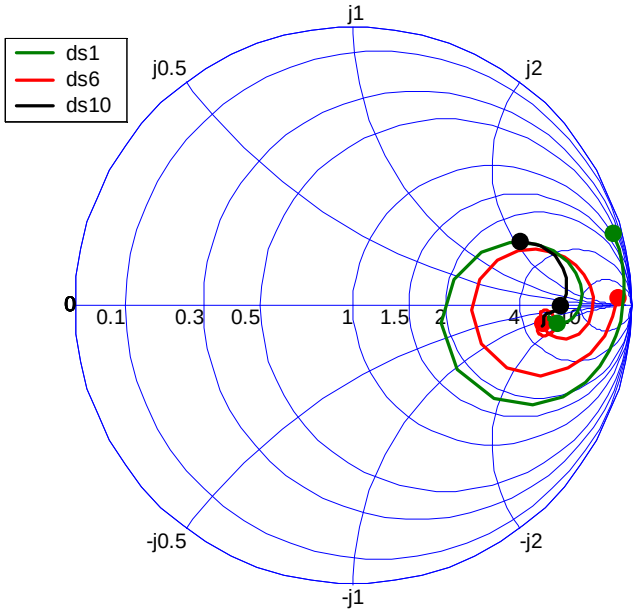

Figure 3.4: Smith chart for ds1, ds6, and ds10, first mark is 2 GHz, second one f_{co}

dimensions in the geometry responsible for the lower frequency.

Upper Frequency Limit

Assuming the upper frequency limit is connected to the dimensions that define the feed point of the antenna, i.e. the point in the center where the spirals deviate from the self-complementary shape, simulations beyond this frequency range were not run. This is because simulations take much longer at these frequencies and because the upper frequency limit of the rectenna will depend also on the package of the nonlinear device that is placed across the feed points. In addition, the transit time of the carriers in the diode may set the upper frequency limit instead of the antenna.

Antenna	Diameter ($\frac{\pi}{2}$ from the end)	Circumference	Frequency
ds1	1.6 cm	5.0 cm	4.7 GHz
ds3	3.8 cm	12 cm	1.9 GHz
ds6	1.5 cm	4.7 cm	5.1 GHz
ds8	2.3 cm	7.2 cm	3.3 GHz
ds10	2.6 cm	8.2 cm	2.9 GHz
ds11	1.5 cm	4.7 cm	5.1 GHz

Table 3.2: Lower frequency limits

3.2 Simulations on the Rectenna

3.2.1 Antenna Model in Circuit Simulation

In general, an antenna is simulated by a power source with a (variable) impedance. The antenna is an infinite resistor for DC, which is simulated by a DC block in the model, as shown in Fig. 3.5. To be able to measure separately the output power of the source and the power reflected from the diode, an ideal three-port is introduced with the following $\mathbf{S}_{3\mathrm{p}}$-Matrix and port impedance vector $\mathbf{z}_{3\mathrm{p}}$. Z is the frequency dependent antenna impedance.

$$\mathbf{S}_{3\mathrm{p}} = \begin{bmatrix} 0 & 0 & 0 \\ 1 & 0 & 1 \\ 0 & 1 & 0 \end{bmatrix}, \qquad \mathbf{z}_{3\mathrm{p}} = \begin{bmatrix} Z^* \\ Z \\ Z^* \end{bmatrix}$$

Ports one and three are matched to the source impedance, i.e. their port impedance is Z^*. The impedance of port two is Z so that voltage and current are the same than at the antenna. The wave leaving port two is made up of the incident power arriving at port one and the reflected power arriving at port three. The reflection occurs in reality between the diode and the antenna, whereas in the model it occurs between the diode and the additional impedance Z connected to port two.

The antenna impedance $Z(f)$ is calculated from $\rho\,(= S_{11})$, which is read from a data file, containing either the results of a simulation or a network analysis.

To be able to simulate antenna characteristics, especially for the frequency dependent transmit antenna, the power level of the source can also be a function of the frequency, i.e. different power levels (measured or computed) can be used over frequency using another data file.

3.2.2 The Rectifier

A diode is soldered directly to the feed point at the center of the antenna. No matching section is used because of area constraints. In the ADS model, the diode is connected to the DC block at port two of the ideal 3-port mentioned, which is part of the antenna model in Fig. 3.5. The DC voltage of the rectenna is measured across the load R_{L}, which is connected to the ends of the spiral arms via 100 nH RF chokes as shown in Fig. 3.6.

Limiting Factors for the Diode Conversion Efficiency

The input power has a strong effect on RF to DC conversion efficiency, which drops sharply once the RF voltage stays below the turn-on voltage of the diode. This is due to the exponential nature of the vi-characteristic of the diode. In fact this was the limiting factor in the cases investigated because input power levels of -5 dBm and below were used.

Another limiting factor is the maximum frequency the diode can work at. It is set by the transit time of the charge carriers, given by the dimensions of the pn-junction and the charge carrier mobility. Even though the transit time for the diodes used is about one order of magnitude lower than $\frac{1}{f}$ in the frequency range investigated, losses in the diode grow significantly with frequency.

3.2.3 Verification

The model was verified on a Vivaldi tapered slot and a spiral antenna. The ρ-parameter of the Vivaldi antenna were obtained by measurement on the network

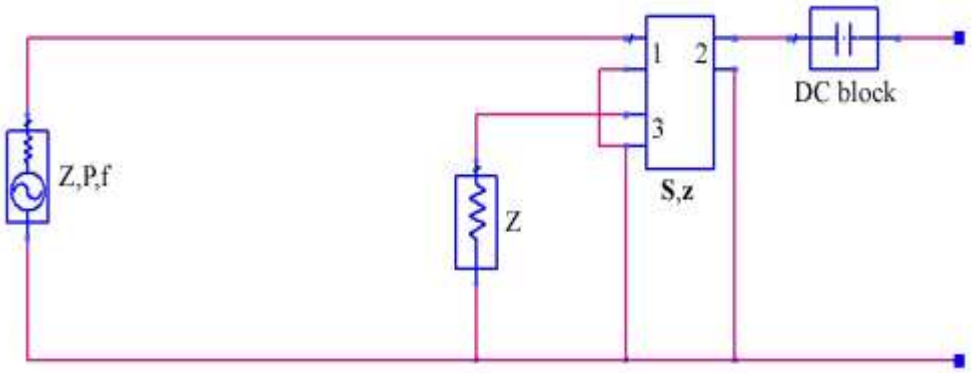

Figure 3.5: The ADS antenna model with ideal 3-port to measure reflected power, power source with parameters antenna impedance Z, power P, frequency f

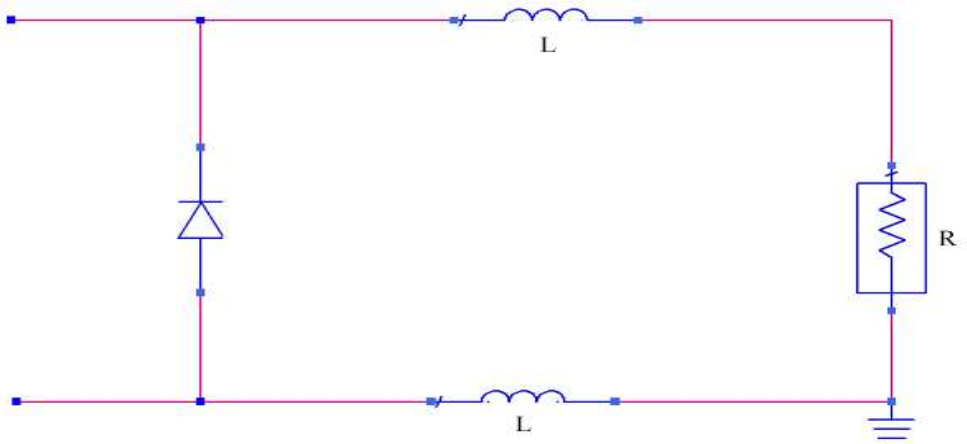

Figure 3.6: The rectification circuit of the rectenna with diode, RF chokes L, and load resistance R

analyzer, whereas the spiral antenna was simulated on IE3D and Ensemble. The measured and simulated DC voltages were compared for different DC loads R_{L}.

Vivaldi

Before connecting a rectifying device to the feed of the Vivaldi antenna, the received RF power into a $50\,\Omega$ input was measured using a power-meter. The result of this measurement was used in the ADS simulation as the power level of the power source in the circuit in order to model the transmit and receive antenna characteristics. Fig. 3.7 shows that in a measurement environment with calibrated incident power and an antenna with measured S-parameters, the model used in ADS is able to predict the shape of the DC output. Only the amplitude of the DC response was not simulated correctly over the entire frequency range. At the second peak, the measurement and simulation deviate by 30% whereas at the fourth peak, deviation was as high as 50%.

Spiral

Fig. 3.8 compares the DC voltage for an open circuit measurement with the ADS simulation results for a load impedance of $10\,\mathrm{M}\Omega$ (voltmeter internal resistance). The input power for the circuit was calculated from the Friis formula

$$\frac{P_{\mathrm{r}}}{P_{\mathrm{t}}} = \left(\frac{\lambda}{4\pi \cdot d}\right)^2 \cdot G_{0\mathrm{t}} \cdot G_{0\mathrm{r}} \tag{3.9}$$

with $G_{0\mathrm{t}}$ the gain of the horn used for measurements, $G_{0\mathrm{r}}$ the directivity of the spiral taken from the simulations, and d the distance between transmitter and rectenna during measurements. The antenna impedance in the ADS model was calculated from Ansoft and Zeland S-parameters. With the power calculated and the simulated S-parameters, it is possible to predict the DC output voltage level. The reason for the steep decrease for higher frequencies is the decreasing rectifier circuit input power, which is explained in chapter 3.3.1. The decreasing input forces the diode

efficiency down, as explained in chapter 3.2.2. The figure shows that the nonlinear rectenna behavior can be predicted by simulations.

3.2.4 Optimal Antenna Impedance

Since no matching network is used, the power reradiated by the antenna depends highly on the mismatch between the antenna and the rectifier circuit. The optimal antenna impedance is the conjugate match of the impedance of the rectifying circuit, i.e. the diode with the RF chokes and the load resistance as mentioned earlier. Because of the dependence of the diode S-parameters on the incident power, however, the optimal impedance is only valid for a certain incident power level. So even in an ideal world, where the antenna would follow the conjugate match of the rectifier, we would have a mismatch for all but one power level, as the antenna impedance is not power dependent, while the diode is. Because the impedance is nearly constant over a certain frequency range for spirals, it would be useful to be able to determine the impedance of the spiral through its shape, and with that being able to locate the spiral impedance at the conjugate match of the diode for a favored frequency and power level.

3.2.5 The Choice of the Diode

When looking for a rectifying diode in the context of RF recycling, a diode with a high conversion efficiency, even for very small incident power levels, is required. The other important point is the matching to the antenna because there is no matching network. So a good trade off is desired between the junction potential V_{j}, the zero bias junction capacitance V_{j0}, the series resistance R_{S}, the saturation current I_{S}, and the sensitivity of the efficiency to mismatch. Fig. 3.9 shows efficiency versus various parameters calculated using Eq. 3.10 given in [McS98], where V_0 is the DC part of the voltage applied to the diode and Θ_{on} the current angle. The figure gives the efficiency for $R_{\mathrm{s}} = 11\,\Omega$, $V_{\mathrm{j}} = 0.4\,\mathrm{V}$, $C_{\mathrm{j0}} = 0.1\,\mathrm{pF}$, $R_{\mathrm{L}} = 1\,\mathrm{k}\Omega$, and $V_0 = 0.3\,V$ at

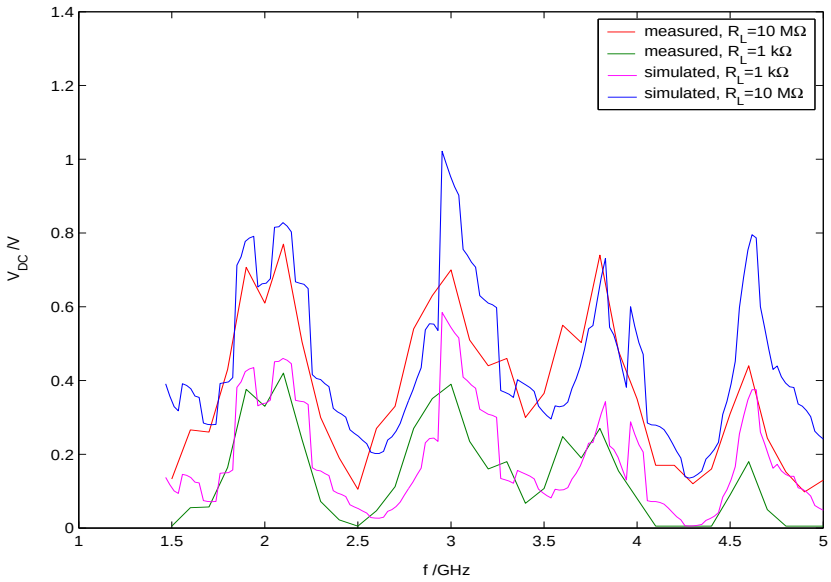

Figure 3.7: Vivaldi rectenna measurement and simulation with calibrated power source and measured antenna impedance

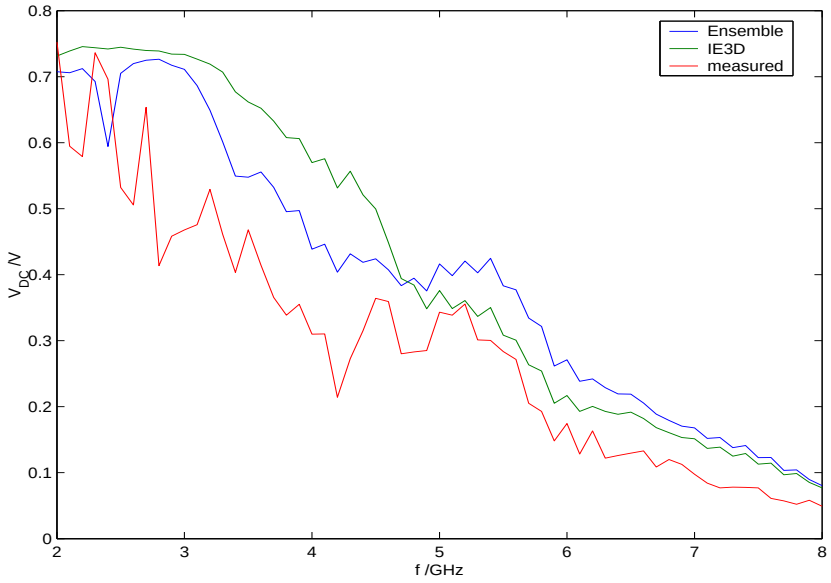

Figure 3.8: Spiral rectenna measurement and simulation with computed power source and computed antenna impedance

a frequency of 4 GHz. One of the parameters R_s, V_j, and C_j0 was varied, whereas all the others were kept constant.

$$
\begin{aligned}
\eta_\mathrm{d} &= \frac{1}{1+A+B+C} \quad \text{with} \\
A &= \frac{R_\mathrm{L}}{\pi R_\mathrm{S}}\left(1+\frac{V_\mathrm{j}}{V_0}\right)^2\left[\Theta_\mathrm{on}\left(1+\frac{1}{2\cos^2\Theta_\mathrm{on}}\right)-\frac{3}{2}\tan\Theta_\mathrm{on}\right] \\
B &= \frac{R_\mathrm{S}R_\mathrm{L}C_\mathrm{j}^2\omega^2}{2\pi}\left(1+\frac{V_\mathrm{j}}{V_0}\right)\left(\frac{\pi-\Theta_\mathrm{on}}{\cos^2\Theta_\mathrm{on}}+\tan\Theta_\mathrm{on}\right) \\
C &= \frac{R_\mathrm{L}}{\pi R_\mathrm{S}}\left(1+\frac{V_\mathrm{j}}{V_0}\right)\frac{V_\mathrm{j}}{V_0}\left(\tan\Theta_\mathrm{on}-\Theta_\mathrm{on}\right) \quad \text{with} \\
C_\mathrm{j} &= C_\mathrm{j0}\sqrt{\frac{V_\mathrm{j}}{V_\mathrm{j}+|V_0|}} \quad \text{and} \quad \tan\Theta_\mathrm{on}-\Theta_\mathrm{on} \approx \frac{\pi R_\mathrm{S}}{R_\mathrm{L}\left(1+\frac{V_\mathrm{j}}{V_0}\right)}
\end{aligned}
\tag{3.10}
$$

The sensitivity of the efficiency to mismatch is displayed in Fig. 3.10, which shows the DC output power, depending on the antenna impedance. The colors show the DC output power and are therefore displaying the sensitivity to mismatch at 1 GHz, whereas the line shows the motion of the optimal impedance from 1 to 15 GHz. The bigger the red hot spot area is, the more insensitive the diode efficiency to mismatch. The data for Fig. 3.10 was calculated by ADS while sweeping the input impedance of the antenna ($\mathfrak{Re}\{Z\} = 0.1\ldots2000\,\Omega$ and $\mathfrak{Im}\{Z\} = 1\ldots2000\,\Omega$) and using the diode Spice-parameters, given by the manufacturer. The input power of the simulation was 3 dBm and the load resistance 600 Ω. The fact that some of the optimal points are identical for different frequencies and the deviation from a smooth curve may be caused by the log-spacing with 10 points per decade that was chosen for the sweep over the impedance.

Three different types of silicon Schottky diodes with parameters shown in Tab. 3.3 were compared with measurements. They were chosen from a variety of available diodes based on simulation results. Measurements suggested the choice of the Alpha Industries SMS7630 over the SMS7621 and the M/ACom MA4E2054. The SMS7630 is not only the most insensitive to mismatch from the diodes measured, but also has the highest conversion efficiency over the frequency range from 2–8 GHz,

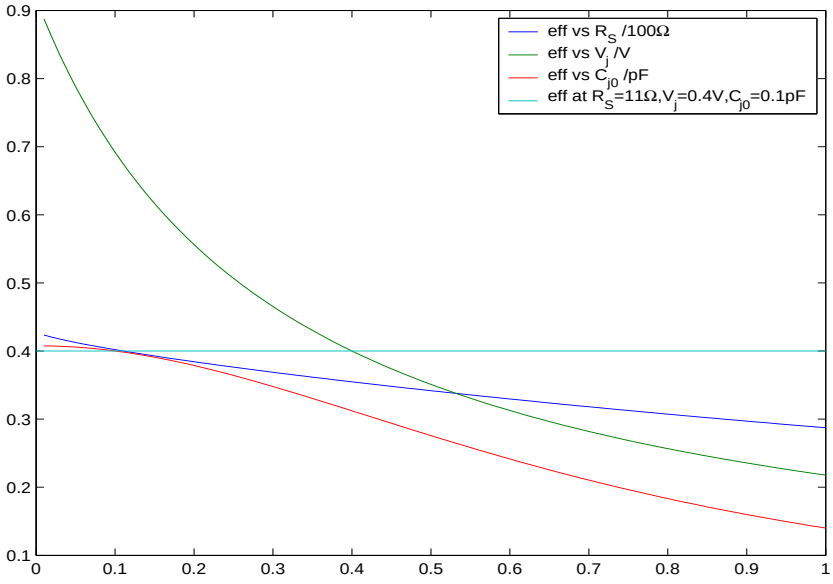

Figure 3.9: Efficiency of a diode vs. various parameters according to Eq. 3.10, one parameter is varied as all others are kept constant

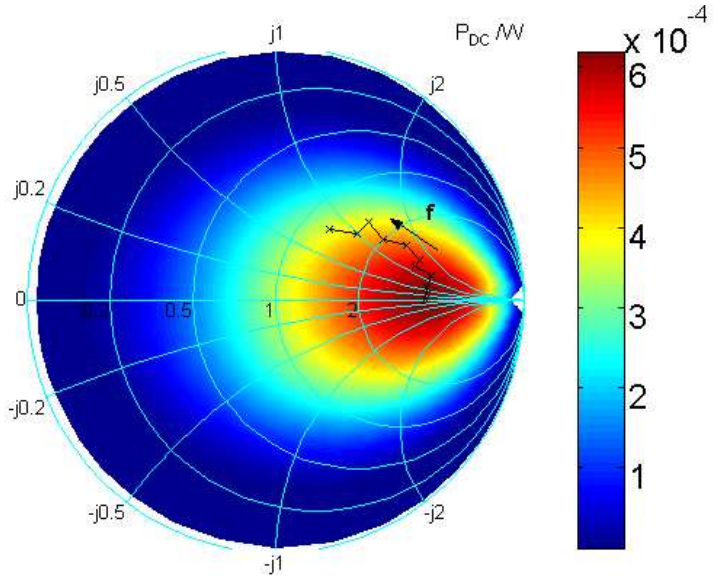

Figure 3.10: Sensitivity to mismatch, antenna impedance is swept over the smith chart and the corresponding DC output power is displayed in color code

see Fig. 3.11. The data in Fig. 3.11 was measured with the diodes soldered into spiral ds3.

Parameter	SMS7630	SMS7621	MA4E2054
I_s /A	$5 \cdot 10^{-6}$	$4 \cdot 10^{-8}$	$3 \cdot 10^{-8}$
R_s /Ω	20	12	11
N	1.05	1.05	1.05
TT /s	$1 \cdot 10^{-11}$	$1 \cdot 10^{-11}$	0
C_j0 /pF	0.14	0.10	0.10
V_j /V	0.34	0.51	0.40
M	0.40	0.35	0.50
E_g /eV	0.69	0.69	0.69
XTI	2	2	-
F_C	0.5	0.5	-
B_V /V	2	3	5.0
I_BV /A	$1 \cdot 10^{-4}$	$1 \cdot 10^{-5}$	$1 \cdot 10^{-5}$

Table 3.3: Diode parameters, as given in manufacturer's specifications

Packaging is another concern when choosing the right diode. Basically, the smallest package is the best choice because of diminished parasitic effects. But as the diodes were soldered onto the antennas, there was a limitation for the size. Diodes measured had SC-79 (max 1.7 mm × 0.9 mm), SOD-323 (max 2.7 mm × 1.35 mm) and SOT-23 (max 2.8 mm × 2.6 mm) packages. Because SOT-23 has a third unused metal connector, which can cause more unwanted effects than the rest of the package, it was not used. Measurements showed no significant differences between the SOD-323 and the SC-79 package. The reason for this might be the frequency range investigated. As the diode is located in the center of the spiral, where mainly high frequencies are received, the packaging would reduce the upper frequency limit of the rectenna. For the 64-element array, SOD-323 was used because of its availability.

3.3 Measurements on the Rectenna

3.3.1 Measurement Setup and Limitations

Measurements were taken in a walk-in anechoic chamber. The transmission antenna was a horn specified for use from 2–18 GHz. The receiving antenna was the rectenna, i.e. the spiral antenna with a diode. The gain of the transmitter was calculated with the Friis transmission Eq. 3.9 using a setup with two identical horns as transmitter and receiver. For this setup the transmitted (P_t) and the received power (P_r) were measured. The distance d between the antennas was chosen, so that far field assumptions could be made, i.e. $d > 2\frac{a^2}{\lambda}$ was obeyed, with a being the maximal aperture dimension. Whenever needed for the Friis equation, the gain for the spiral was extracted from either IE3D or Ensemble simulations. It was only used for 1D, i.e. broadside measurements. Each data-point consists of at least a DC voltage, i.e. the DC output of the rectenna, and was taken versus at least one of the following variables: transmitted power P_t, frequency f, elevation angle ϑ, or azimuth angle φ. Fig. 3.12 shows the measurement setup. For 1D measurements, the motors remain stationery. For 2D-polarization, only one of the two φ-motors is turned, whereas for 3D-measurements the ϑ-motor is turned and both φ-motors are turned simultaneously.

Measurements on the rectenna were limited by the amplifier available (2–8 GHz, 30 dB gain, max 30 dBm) and the distance necessary between the transmit antenna and the spiral to guarantee far-field measurements.

1D Setup

For 1D measurements, transmitter and receiver had a fixed position with their broadsides facing and the parameters frequency and power varied. To calculate the received power of the spiral, the Friis equation (3.9) was used. The broadside gain of the horn is known, as mentioned earlier, and the directivity of the spiral was taken

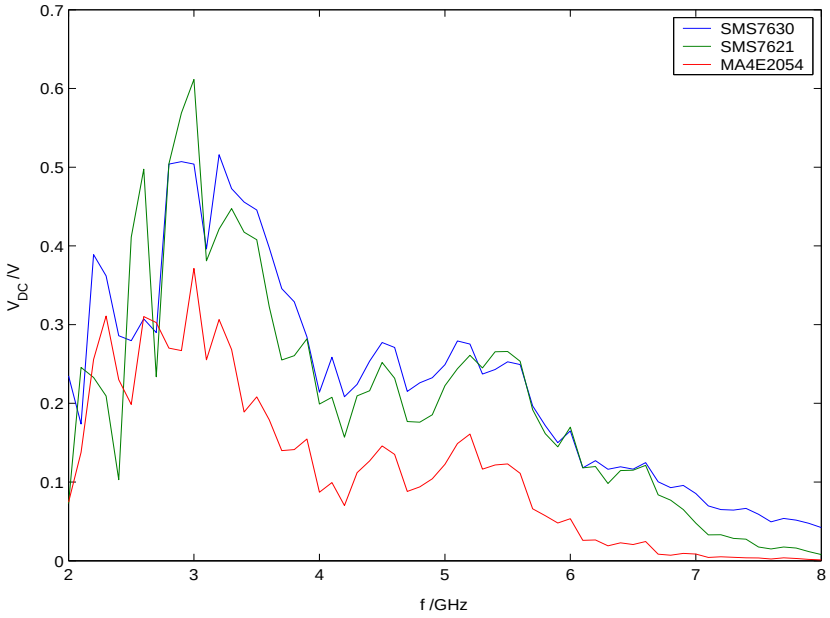

Figure 3.11: Comparison of the Diodes

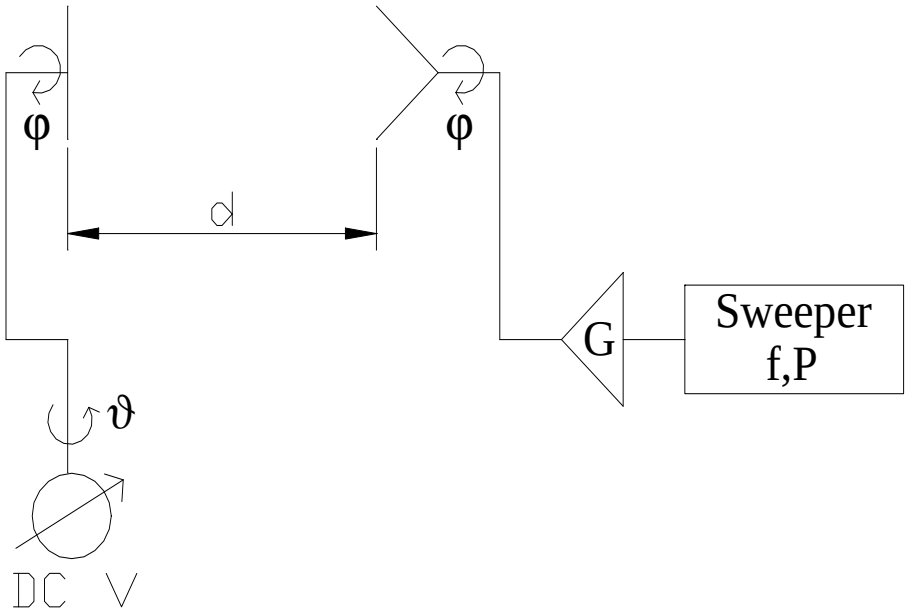

Figure 3.12: Measurement setup in the anechoic chamber

from the simulations.

2D Polarization Setup

For 2D measurements, the azimuth angle φ was swept over the range $0 \leq \varphi \leq \pi$, with $\varphi = 0$ specifying the x-axis. The polarization of the spiral is in theory perfectly point-symmetric to the the spiral center, so a sweep over an angle π delivers all the information.

3D Setup

For 3D measurements, ϑ and φ were varied, with $0 \leq \vartheta \leq \frac{\pi}{2}$ and $0 \leq \varphi < 2\pi$. By changing those two variables, data-points on the surface of a complete hemisphere can be taken. Every measurement was taken twice, with the polarization of the transmitter turned $\frac{\pi}{2}$ from the first case. The hemisphere was measured with a resolution of at least 648 points with $N_\varphi = 50$, i.e. 50 points at the equator, and $N_\vartheta = 20$. The sample points have near-constant spacing. Fig. 3.13 shows the distribution of 648 points over a hemisphere.

3D Reradiation Setup

To measure reradiated harmonics, a second horn is needed to receive the reradiated power of the harmonics. This antenna is connected to the spectrum analyzer. A data-set consists of five measured values here, DC voltage, power of the fundamental, 2nd, 3rd, and 4th harmonics. Other than in the above mentioned setup, the position of the spiral relative to the transmission horn does not change. It illuminates the rectenna from a point on the -z axis. So in order to get the reradiated power of the rectenna, the measured power levels are added up and multiplied by two because only one hemisphere was measured. This is of course only possible for planar antennas, that have symmetric patterns, relative to the plane they lie in.

3.3.2 Efficiency versus Incident Power

As mentioned earlier, the rectifying efficiency of the diode depends on the amount of incident power. The 1D-measurement at a fixed frequency of 4 GHz does not only show this dependence, but gives also an idea about the overall efficiency that can be reached with the spiral investigated. As the graph shows efficiency only for one frequency point, a frequency point with average efficiency was chosen. For this measurement the cables and the amplifier that are in the path between the sweeper and the transmission horn were calibrated from -15 dBm to 5 dBm sweeper output power. The sweeper output power, corrected by the calibration result, was then used to calculate the incident power of the rectenna, as mentioned in chapter 3.3.1. The distance between transmitter and rectenna was $d = 0.6\,\mathrm{m}$, and the load resistance $R_\mathrm{L} = 600\,\Omega$. Fig. 3.14 shows that the efficiency increases slowly but steadily with power at roughly 14 dB per decade of incident power. The decrease in efficiency for the measured curve at extremely low incident power levels might be a result of the proximity of the noise floor. The simulated curve, based on IE3D S-parameters, shows a steep increase first, then a leveling off and finally a slight decrease. The increase is a result of the exponential vi-curve of the diode, whereas the decrease for high power levels is caused by two factors: the first is the RF voltage approach to the reverse breakdown voltage during the high impedance state of the diode. The second factor is the diode current as it approaches the saturation current of the diode during the low impedance state.

The graph shows that the overall efficiency is somewhere between 2 and 8 percent, due mostly to the mismatch between diode and antenna. RF rectifiers with only one diode can reach efficiencies well above 60%, as proven by Figs. 2.7 and 2.8. For the rectenna used for this measurement (ads3), efficiencies up to 15% were calculated, depending on the frequency. It is important to mention here that calculating the received power needed to express efficiency is subject to an error on the order of 10% or more because the figure depends on the directivity of the

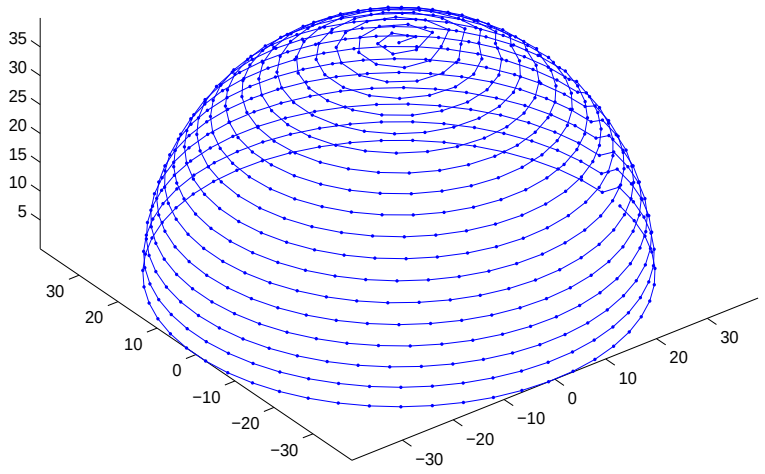

Figure 3.13: Hemisphere with 648 points ($N_\varphi = 50$, $N_\vartheta = 20$), constant spacing

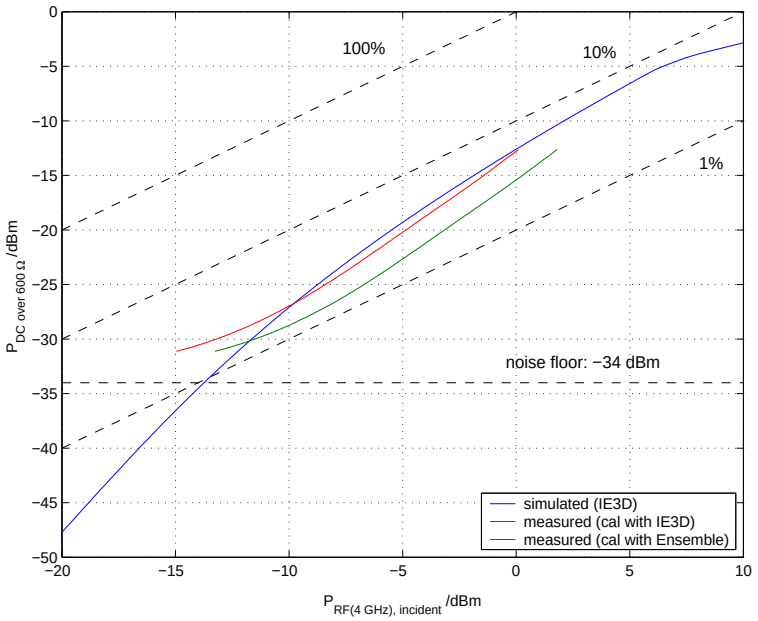

Figure 3.14: Efficiency versus incident power (ads3)

spiral taken from the simulations. Conversion efficiency is subject to an even higher error because of the difficult task of measuring reflected power on the fundamental frequency and so is not mentioned here.

3.3.3 Polarization

In Fig. 3.15 the polarization of spiral ads3 is plotted for 2, 3, and 7 GHz. It shows DC power versus the azimuth angle of the rectenna. The distance between transmitter and rectenna was $d = 0.6\,\mathrm{m}$ and the load resistance $R_\mathrm{L} = 600\,\Omega$. This data comes from a 2D-polarization measurement. Each trace is normalized to its maximum and shows clearly that for frequencies below $f_\mathrm{co} \approx 5\,\mathrm{GHz}$ the spiral is linearly polarized, with the direction changing over frequency. Above f_co the polarization becomes circular.

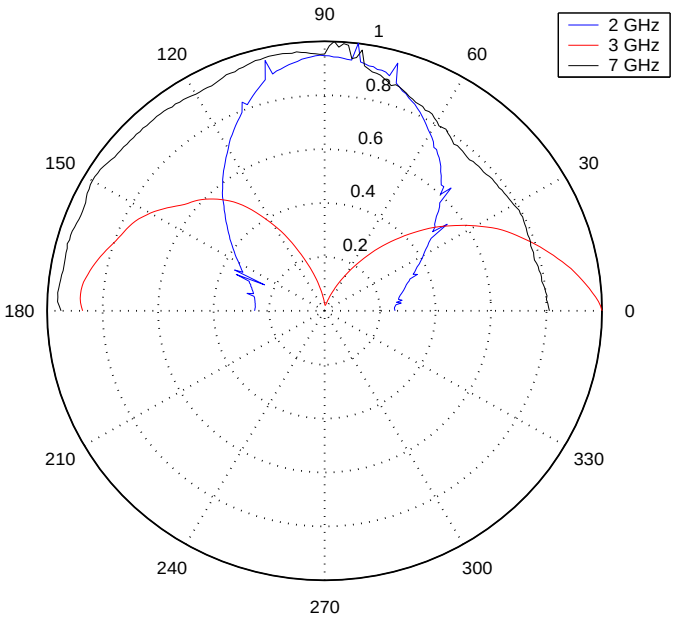

Figure 3.15: Polarization of spiral ads3

3.3.4 3D DC Pattern

Figs. 3.16 and 3.17 show the DC power gained from incident waves over one hemisphere. The data-points displayed are the sum of the two measurements with both orientations of the transmitter. The distance between transmitter and rectenna was $d = 0.6\,\mathrm{m}$ and the load resistance $R_\mathrm{L} = 600\,\Omega$. The resolution was 648 points per hemisphere for both measurements. The power is normalized to the maximum, which is on the order of several hundred μW. More exactly, the maximum for 3 GHz was -1.3 dBm and -13 dBm for 6 GHz. The 3D DC pattern shows roughly the pattern of the antenna. It does not exactly correspond with the antenna pattern because the diode efficiency depends on the received power. Still, the antenna pattern is supposed to look roughly like the pattern shown.

For 3 GHz the spiral is still linearly polarized. There are two main polarization directions which are $\varphi = \frac{\pi}{4}$ and $\varphi = \frac{3\pi}{4}$. At these azimuth angles the spiral outputs nearly as much power at $\vartheta = \frac{\pi}{2}$ than it does at $\vartheta = 0$. The power rectified at these angles is some 15–20 dB higher than for other azimuth angles. At 6 GHz the pattern becomes smoother. There are two reasons for this: first, the noise-floor is closer, i.e. the maximum is only about 20 dB above the noise. Second, the polarization becomes circular, as 6 GHz is close to the calculated f_co of the spiral.

3.3.5 Reradiation of Harmonics

The reradiated power of the 1st, 2nd, 3rd, and 4th harmonics was measured as described in chapter 3.3.1 over one hemisphere in both polarizations for a 3 GHz incident wave. The distance between transmitter and rectenna as well as the distance between receiver horn and rectenna was $d = 0.6\,\mathrm{m}$. The load resistance was $R_\mathrm{L} = 600\,\Omega$. So the numbers for the reradiated power displayed in blue in Fig. 3.18 are 2×648 data-points for two orthogonal incident polarizations added up and multiplied by $\frac{4\pi}{\lambda^2 \cdot G_\mathrm{r}}$. This factor takes the changing effective aperture of the receiving horn into

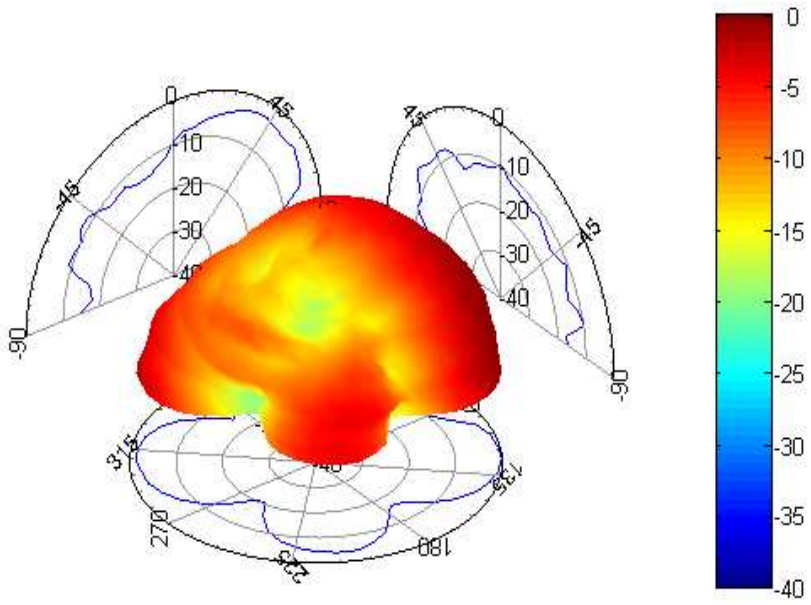

Figure 3.16: DC pattern of spiral ads3 at 3 GHz

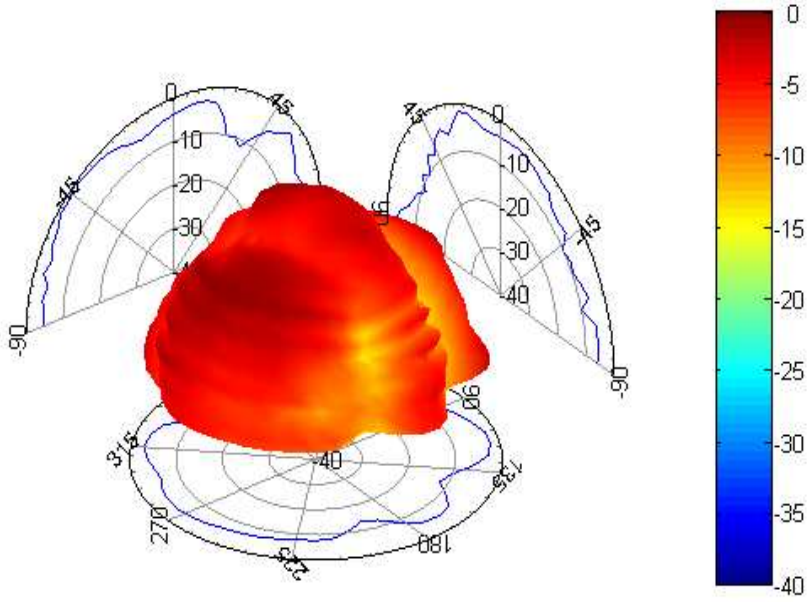

Figure 3.17: DC pattern of spiral ads3 at 6 GHz

account (see Eq. 3.11). The total power reradiated on each of these frequencies is even another 3 dB higher (red line) than the measurement results because the spiral radiates in both z half-spaces. As DC power was measured directly at the spiral via wires, it is only added up without the radiation factor. The incident power was calculated as mentioned in chapter 3.3.1, the error bar resulting from different directivity values from IE3D and Ensemble. The incident power may be even higher because of mounting structures for the rectenna that hold it in front of the transmitter and might act as scatterers. The power given as re-radiation on the 1st harmonic here is not only made up from re-radiation, but also from radiation that goes directly from the transmitting horn to the receiver horn. These reasons could explain the fact that the reradiated power is higher than the received, as predicted by Ensemble. Another approach to this result is the error of the simulation as Ensemble predicts a broadside gain for the spiral of only 1 dB. All numbers are normalized to the calculated (IE3D) incident power.

The summation of the measured power-levels can be seen as an approximation of the integration of the received power over a hemisphere. As the spiral has symmetric patterns in the +z and -z half-space, the integrated power over a sphere is simply 3 dB higher than for a hemisphere. Integrating the Friis equation and using the general expression for the directivity given by [Bal97] yields:

$$\begin{aligned} \int\limits_{\partial V_{\text{sphere}}} P_{\text{r}} \cdot dA &= P_t \cdot G_{\text{r}} \frac{\lambda^2}{(4\pi)^2} \cdot \int\limits_0^{2\pi} \int\limits_0^{\pi} G_{\text{t}} \cdot \sin(\vartheta) \cdot d\vartheta d\varphi = P_t \cdot G_{\text{r}} \frac{\lambda^2}{4\pi} = \\ &= \lim_{N_\varphi, N_\vartheta \mapsto \infty} \sum_{k=1}^{N_\varphi} \sum_{l=1}^{N_\vartheta} P_{k,l} \cdot \Delta A(k,l) \end{aligned} \tag{3.11}$$

G_{r} is independent of φ and ϑ because it is always the broadside of the receiving horn that faces the center of the sphere, i.e. the rectenna. Fig. 3.19 shows the sum of both measurements over φ and ϑ. The data is normalized to -44.1 dBm.

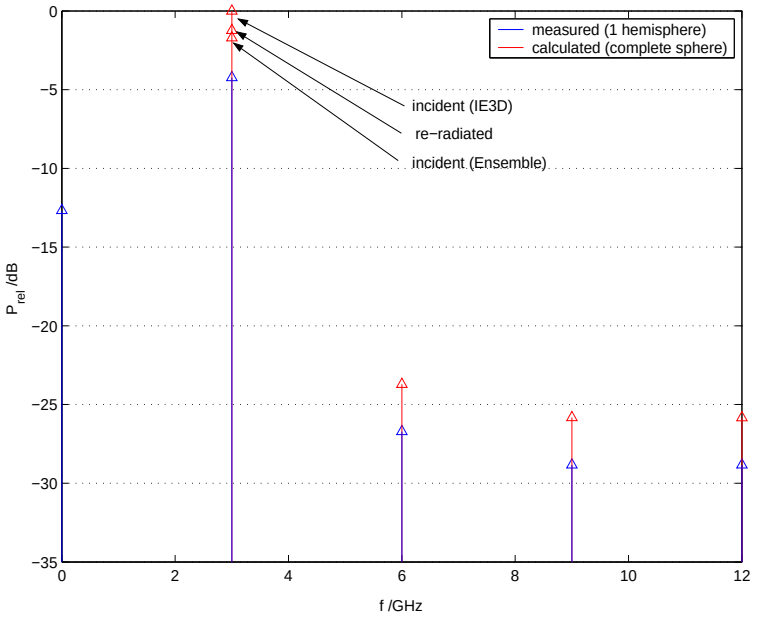

Figure 3.18: Spectrum of the reradiated power (spiral ads3)

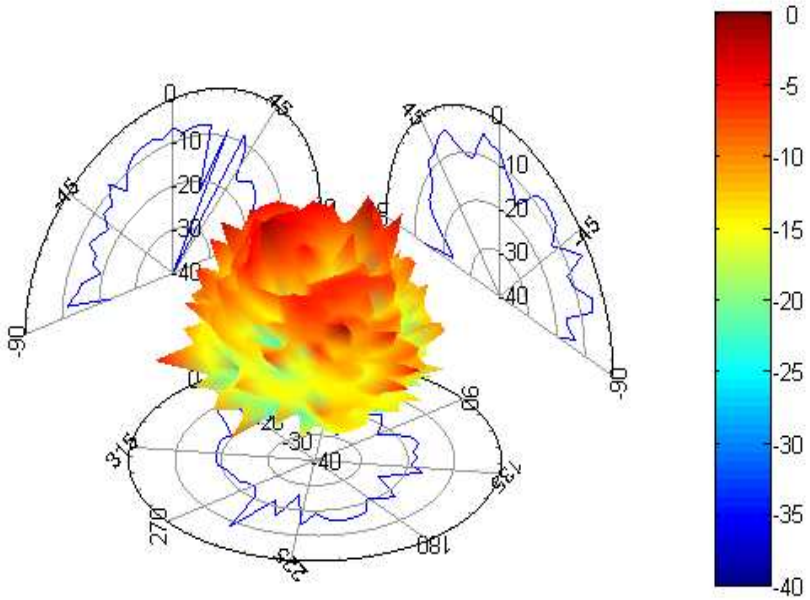

Figure 3.19: Distribution of the power reradiated on the 3rd harmonic (spiral ads3)

Chapter 4

A Rectenna Array

4.1 Design

There are two major questions about rectenna array design, once the single element is chosen: one is the question of series or parallel DC connection of the elements and the second one is array lattice design. Optimal includes on the one hand a high density of rectenna elements and on the other hand variations of orientation of the spiral so that many possible polarizations can be received. The single element chosen for the arrays is ads3.

4.1.1 2 by 2 Elements Array

In this array, two rectennas in series are connected in parallel to another two in series. This means that the DC impedance of the array is the same as that of a single element. Because the spiral is circularly polarized above a certain frequency, one pair of the spirals in series was placed to receive LHCP whereas the other pair receives RHCP.

For the placement, a very simple solution was chosen. The array element consists of four elements arranged in a rectangle with two elements for each circular polarization. This might not be the best solution, as far as packing density is

concerned, but it is very easy to create a larger array on the basis of this 2×2 array. The array has a size of $50 \times 40\,\mathrm{mm}^2$. This includes two small pads that are designed to connect to wires.

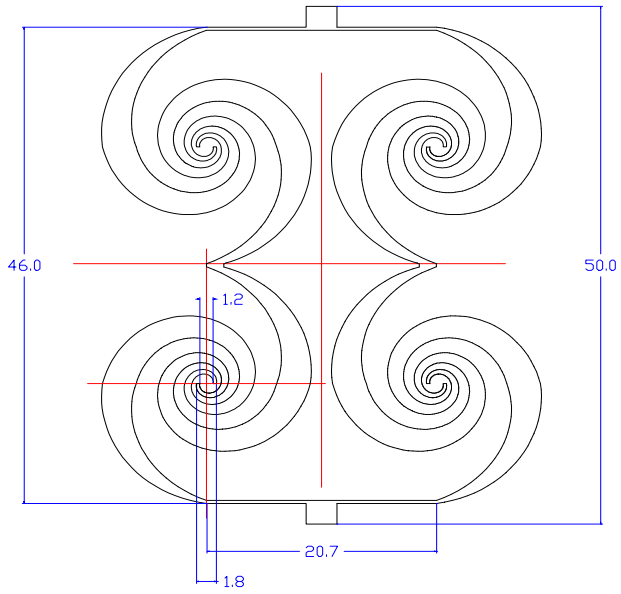

Figure 4.1: Dimensions of the 2×2 array, a pair of series spirals in parallel to another one

The array was milled on a Rogers Duroid substrate ($\epsilon_\mathrm{r} = 2.2$, $\mu_\mathrm{r} = 1$), 20 mil (=0.508 mm) thick, with a 1 oz copper layer ($\approx 35\,\mu$m).

4.1.2 4 by 4 Elements Sub-Array

This sub-array of the 8×8 array consists of four 2×2 blocks. Each of these 4 blocks has an orientation that differs $\frac{\pi}{2}$ from its predecessor. With that placement not only LHCP and RHCP can be received but also horizontal and vertical polarizations for low frequencies, where the spirals are linearly polarized. By now the rotation and mirroring of the single elements costs 3 dB for every incident polarization because at half the elements have the wrong polarization. The advantage of this combination

is that there should not be any deep nulls because of the same reason. The four 2×2 blocks from chapter 4.1.1 that make up this array are connected in parallel to better match the rectenna to lower load resistances.

4.1.3 8 by 8 Elements Array

This array consists of 4 elements of the 4×4 sub-array. Again each element has an orientation that differs $\frac{\pi}{2}$ from its predecessor. The 4 elements are not connected by hard-wires, to keep the chance of changing the connections. The connections are wires soldered to small pads on the sub-arrays.

The array was etched on a Rogers Duroid substrate ($\epsilon_\mathrm{r} = 2.2$, $\mu_\mathrm{r} = 1$), 10 mil (=0.254 mm) thick, with a $\frac{1}{2}$ oz copper layer ($\approx 18\,\mu$m). This substrate was chosen because of its thinner copper layer, which makes etching faster and therefore protects the thin DC lines better. Fig. 4.2 shows the layout of the array with overall dimensions of $185 \times 185\,\mathrm{mm}^2$.

4.2 Measurements

4.2.1 3D DC Pattern of the 2 by 2 Elements Array

Figs. 4.3 and 4.4 show the DC pattern of the 2×2 array. They are smoother than the patterns for the single element. In addition, even for 3 GHz, the array receives roughly the same amount of power for every orientation. 0 dB correspond to 0 dBm for the 3 GHz plot and to -14 dBm for 6 GHz. This shows that the array-factors need not to be taken into account for rectennas as the power is higher at every point than for a single element, where the same distance between transmitter and rectenna was used. This is because the power is combined at DC. Combing DC power means that there is no phase which can cause destructive interference. The distance between transmitter and array was $d = 0.6\,\mathrm{m}$ and the load-resistance $R_\mathrm{L} = 600\,\Omega$.

Figure 4.2: Layout of the 8×8 array with 64 diodes (black devices), 4×4 sub-arrays are not wired here, dimensions $185 \times 185\,\mathrm{mm}^2$

4.2.2 3D DC Pattern of the 8 by 8 Elements Array

The patterns of the 8×8 array are a lot smoother than those for the 2×2 array. 0 dB correspond to 8.5 dBm for the 3 GHz plot and to -8.1 dBm for 6 GHz. The distance between transmitter and array was $d = 1.2\,\mathrm{m}$ and the load-resistance $R_\mathrm{L} = 80\,\Omega$. The measurements were taken with the 4×4 sub-arrays connected in parallel by wires.

4.2.3 Broadside Power Sweep Comparison

This 1D-measurement compares the DC power output of the 8×8 (ar6) and 2×2 (ar3) arrays with the single element ads3. DC output is compared over the power density at the location of the rectenna. The 2×2 array and the single element had a distance of $d = 0.6\,\mathrm{m}$ between transmitter and rectenna and a load resistance of

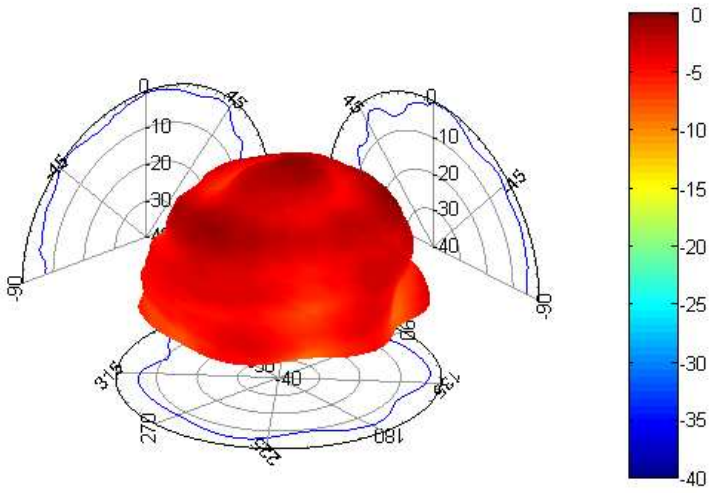

Figure 4.3: 3D DC pattern of the 2×2 array at 3 GHz

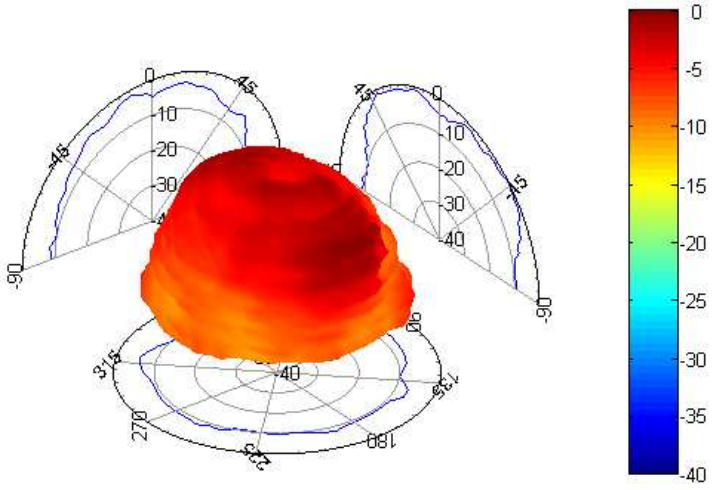

Figure 4.4: 3D DC pattern of the 2×2 array at 6 GHz

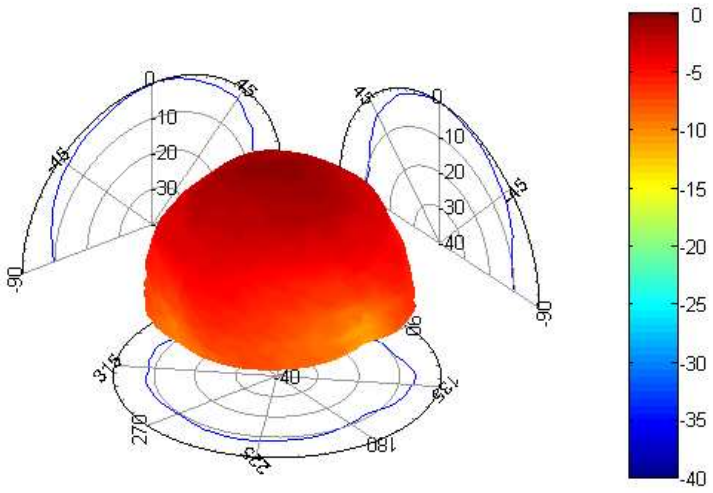

Figure 4.5: 3D DC pattern of the 8×8 array at 3 GHz

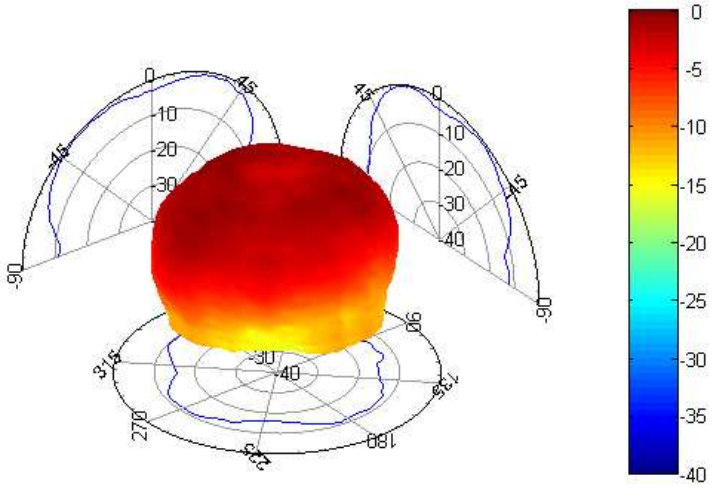

Figure 4.6: 3D DC pattern of the 8×8 array at 6 GHz

$R_{\mathrm{L}} = 600\,\Omega$. The 8×8 array was measured three times, once all four sub-arrays were connected in parallel, once in series and once two elements in series were parallel to another two in series. The distance between transmitter and rectenna was $d = 1.2\,\mathrm{m}$ and the load resistance $R_{\mathrm{L}} = 80\,\Omega$ for the parallel case, $R_{\mathrm{L}} = 600\,\Omega$ for the series case and $R_{\mathrm{L}} = 200\,\Omega$ for the mixed one. The resistances were chosen manually for the highest output power. The left end of each trace shows the bend, where the DC output climbs above the noise floor. The high noise floor results from the stage motors in the anechoic chamber.

The figure shows, that a parallel connection of the sub-arrays performs about 2 dB better than a series parallel combination and even 4 dB better than a series connection. The advantage of the 8×8 array with parallel connection over the 2×2 array is roughly 16–20 dB. It goes along with an increase of the physical aperture by a factor of 16 which is 12dB. This means an increase in effective efficiency of 4–8 dB. The output power of the 2×2 array is again 8 dB higher than for a single element with the area increasing only 6dB and resulting in an effective increase of efficiency of roughly 2 dB. Increase of efficiency with incident power is also different for the three compared cases. The single element shows an increase of roughly 15 dB per decade of incident power density, the 2×2 array 18 dB per decade, and the 8×8 array 17 dB per decade. This figures represent only the broadside case, which was measured here.

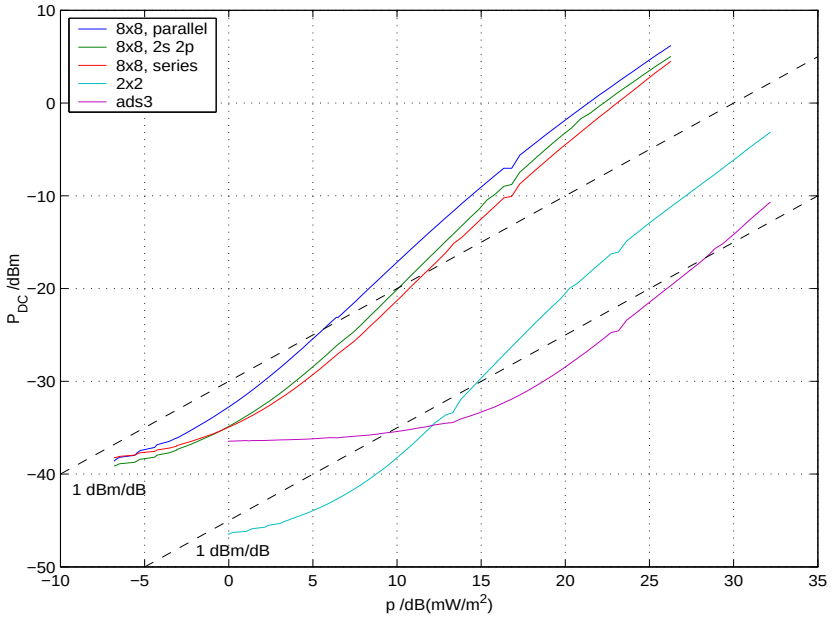

Figure 4.7: Comparison of DC output power vs. power density

Chapter 5

Conclusion and Future Work

As a conclusion of this work there are two main aspects to mention. First this work shows that a rectenna can be simulated using harmonic balance simulation for the circuit and electromagnetic simulators for the antenna part. Second, the measured results presented indicate that rectennas might work as RF recyclers with an output power level high enough to be efficiently stored and reused.

Further investigations would include devices that are able to collect and store energy from power levels that correspond to the rectenna output. Shrinking the size of the rectenna is another aspect, that requires more work. The frequency behavior might stay constant if the ϵ_r of the substrate increases with the decreasing size of the antenna, but the package size of the diode will stay constant. More measurements, especially at frequencies higher than 8 GHz, will produce interesting results. From these investigations, conclusions can be drawn to the upper frequency limit of the antenna and the diode as well as the influence of the diode package. Furthermore, measurements of situations with more than one incident frequency, as they occur in real life, can be done. Two incident waves with different frequencies can interfere destructively as well as constructively.

Bibliography

[Bal97] Constantine A. Balanis. *Antenna Theory.* John Wiley & Sons, New York, 2nd edition, 1997.

[Edw88] T.C. Edwards. *Foundations for Microstrip Cicuit Design.* John Wiley & Sons, Chichester, 1988.

[Ell62] R. S. Elliot. A View of Frequency Independent Antennas. *Microwave Journal*, pages 61–68, December 1962.

[Hag] Joseph A. Hagerty. *Simulations for a High-Efficiency rf-dc Rectifier and Integration in a Microwave dc-dc Converter.* Department of Electrical and Computer Engineering, University of Colorado, Boulder, CO 80309-0425, USA.

[Hal86] P. S. Hall. Multioctave bandwidth log-periodic microstrip antenna array. In *IEEE Proceedings*, volume 133, pages 127–136s, April 1986.

[HP01] Joseph A. Hagerty and Zoya Popović. An Experimental and Theoretical Characterization of a Broadband Arbitrarily-Polarized Rectenna Array. In *IEEE Transactions on Microwave Theory and Techniques*, pages 1855–1858, 2001.

[JDDM64] E. C. Jordan, G. A. Deschamps, J. D. Dyson, and R. E. Mayes. Developments in broadband antennas. *IEEE Spectrum*, pages 58–71, April 1964.

[Joh92] Richard C. Johnson, editor. *Antenna Engineering Handbook*, chapter 14. McGraw-Hill, Inc., New York, 3rd edition, 1992.

[Maa97] Stephen A. Maas. *Nonlinear Microwave Circuits*. IEEE Press, New York, 1997.

[McS98] James O. McSpadden. *Rectifying and Oscillating Integrated Antennas*. PhD thesis, Texas A&M University, 1998.

[MFC98] James O. McSpadden, Lu Fan, and Kai Chang. Design and Experiments of a High-Conversion-Efficiency 5.8 GHz Rectenna. In *IEEE Transactions on Microwave Theory and Techniques*, volume 46, pages 2053–2060, December 1998.

[MYC92] James O. McSpadden, Taewhan Yoo, and Kai Chang. Theoretical and Experimental Investigation of a Rectenna Element for Microwave Power Transmission. In *IEEE Transactions on Microwave Theory and Techniques*, volume 40, pages 2359–2366, December 1992.

[Nah75] Joseph J. Nahas. Modeling and Computer Simulation of a Microwave-to-DC Energy Conversion Element. In *IEEE Transactions on Microwave Theory and Techniques*, pages 1030–1035, 1975.

[PN85] B. D. Popović and A. Nĕsić. Some extensions of the concept of complementary electromagnetic structures. In *IEEE Proceedings*, volume 132, pages 131–137, April 1985.

[RTB98] Ralph H. Rasshofer, Markus O. Thieme, and Erwin M. Biebl. Circularly Polarized Millimeter-Wave Rectenna on Silicon Substrate. In *IEEE Transactions on Microwave Theory and Techniques*, volume 46, pages 715–718, May 1998.

[Rum57] V. H. Rumsey. Frequency Independent Antennas. *I.R.E. National Convention Record, Part I*, pages 114–118, 1957.

[SM98a] Naoki Shinohara and Hiroshi Matsumoto. Dependence of dc Output of a Rectenna Array on the Method of Interconnection of Is Array Elements. *Electrical Engineering in Japan*, 125:9–17, 1998.

[SM98b] Naoki Shinohara and Hiroshi Matsumoto. Experimental Study of Large Rectenna Array for Microwave Energy Transmission. In *IEEE Transactions on Microwave Theory and Techniques*, volume 46, pages 261–267, March 1998.

[YC92] Tae-Whan Yoo and Kai Chang. Theoretical and Experimental Development of 10 and 35 GHz Rectennas. In *IEEE Transactions on Microwave Theory and Techniques*, volume 40, pages 1259–1266, June 1992.